



# Parametric study of instabilities in three-dimensional hypersonic flows

Thomas Zielinski<sup>1</sup>, José Cardesa<sup>1</sup>, Guillaume Bégou<sup>2</sup>, Jean-Philippe Brazier<sup>1</sup>, Laurent Muscat<sup>2</sup>, Marina Olazabal-Loumé<sup>3</sup>

#### **Abstract**

Boundary layer transition is of particular interest in the prediction of the aerodynamic performances and maneuverability of a given hypersonic vehicle. However, it has been found to be highly sensitive to flow parameters such as the Mach number, unit Reynolds number, cross-flow effects and wall temperature. Besides, from a numerical point of view, it is particularly difficult to obtain representative boundary-layer profiles to understand and then model these effects on the dominant instability modes. In this paper, a methodology relying on metric-based mesh adaptation has been validated and applied to address these issues. More specifically, the effects of the unit freestream Reynolds number, the wall temperature ratio  $T_w/T_r$  and the angle of attack on various boundary layer profiles and the typical instability waves (crossflow instability, first and second Mack modes) for a sharp 7-degree cone geometry are investigated. It has been observed that the increase in unit Reynolds number destabilizes all modes. Moreover, it was shown that the ratio  $T_w/T_r$  has a drastic effect on these modes. Indeed, although the second Mack mode is strongly destabilized when lowering the  $T_w/T_r$  ratio, the highly oblique modes behaved in the opposite fashion, being strongly destabilized with an increase of  $T_w/T_r$ . Below  $T_w/T_r \approx 0.3$ , the first mode became completely stable and the crossflow mode was always unstable for all the chosen  $T_w/T_r$  values. Finally, it has been found that the angle of attack significantly destabilized the crossflow instability by increasing the values of  $|w_{max}/U_e|$  and the variation of edge quantities across the flowfield due to a stronger azimuthal pressure gradient induced by the curved bow shock.

Keywords: boundary-layer transition, hypersonic, flow stability, three-dimensional flows.

### **Nomenclature**

#### Latin

u - Longitudinal velocity v - Wall-normal velocity w - Transverse velocity

p - Pressure T - Temperature

 $T_0$  – Stagnation temperature

M - Mach number Re - Reynolds number AoA - Angle of attack

GIP - Generalized inflexion point

 $T_w$  — Wall temperature s — Curvilinear abscissa  $R_N$  — Nosetip radius  $L_c$  — Cone length f — Frequency

 $m\,-\,$  Non-dimensional azimuthal wavenumber

x, y, z - Spatial coordinates

# Greek

 $\theta_c$  – Cone half angle

 $\phi$  – Azimuthal angle around the cone

 $\mu$  - Molecular viscosity

 $\alpha$  – Streamwise wavenumber

 $\beta$  - Transverse wavenumber

n - Normal body-fitted coordinate

 $\xi$  – Streamwise body-fitted coordinate

 $\zeta$  – Transverse body-fitted coordinate

 $\omega$  – Angular frequency

 $\alpha_i$  – Amplification rate

 $\sigma$  – Growth rate

# Subscripts

 $\infty$  – Freestream values

e - Boundary layer edge values

u - Regarding the longitudinal velocity

w - Regarding the crossflow velocity

<sup>&</sup>lt;sup>1</sup>DMPE, ONERA, Université de Toulouse, 31000, Toulouse, France

<sup>&</sup>lt;sup>2</sup>DAAA, ONERA, Institut Polytechnique de Paris, 92190, Meudon, France

<sup>&</sup>lt;sup>3</sup>CEA CESTA, 15 Avenue des Sablières CS60001, 33116, Le Barp CEDEX, France

### 1. Introduction

The design of hypersonic vehicles requires a precise estimation of the heat fluxes at the wall, which depend on the laminar or turbulent state of the boundary layer. Considering that the boundary layer state affects the overall aerodynamic performance of the vehicle, being able to predict the flow transition is of prominent importance. Recent design concepts require taking into account longitudinal instabilities but also three-dimensional ones such as the crossflow instability, which is particularly difficult to characterize and model. As a result, three-dimensional effects must be accounted for in transition modeling.

Moreover, the equations to be solved in order to generate reliable boundary-layer profiles are crucial in the hypersonic regime. Indeed, Paredes *et al.* [1] have shown that the solutions obtained from the stationary Navier-Stokes equations and self-similar solutions led to significant differences, especially in the stability results. They found that the full Navier-Stokes solutions tended to predict a delayed transition compared to self-similar solutions coupled to an inviscid or viscous solution for the region outside of the boundary layer. The disagreement results from assuming certain simplifications that deteriorate the representativeness of the boundary layer profiles, the stability results and hence the prediction of the transition onset. Thus, choosing a strategy completely based on solving the Navier-Stokes equations is of particular interest to improve our understanding of these instabilities in three-dimensional flows. However, it is fair to say that generating a 3D mesh with suitable shock alignment and resolution is extremely time-consuming. Consequently, a first study involving metric-based mesh adaptation for the base flow computation followed by stability analysis has been investigated. Our fully automatic approach has been validated by comparing stability results from the literature for both the Mack modes and the crossflow instability, leading to an excellent agreement.

Furthermore, the effect of freestream conditions must also be considered in order to accurately predict the flow transition in a wide range of flow conditions, thus allowing a model to be both precise and robust in an entire trajectory. For example, for the HIFIRE-5 blunt elliptic cone geometry, it has experimentally been shown by Juliano et al. [2] that the freestream unit Reynolds number had a significant influence on the location of the transition onset for both quiet and noisy flow. Furthermore, it has also been shown that the angle of attack, usually known to destabilize the crossflow instability, can actually stabilize and destabilize this instability on the windward and leeward face respectively, thus highlighting the prominent effect of the angle of attack. Besides, Mack [3] has shown that the Mach number has a prominent role in the transition of laminar flows. For an adiabatic flat plate, the author [3] has for instance shown that the second Mack mode prevailed over the first Mack mode when  $M_e > 4$ , thus proving that the mechanisms of transition are highly dependent on the Mach number. Moreover, it has also been found that these two specific modes are highly sensitive to the wall temperature ratio  $T_w/T_r$ . Indeed, the first and second Mack modes are respectively stabilized and destabilized for a colder wall case usually representative of flight data where an extremely cold wall can even completely stabilize the first Mack mode but at the cost of significantly destabilizing the second Mack mode. As a result, it appears evident that the freestream parameters  $M_{\infty}$ ,  $Re_{\infty}$ ,  $\alpha$  and  $T_w/T_r$  must be quantitatively investigated and accounted for in transition modeling. In this study, the aforementioned validated and automatic metric-based mesh adaptation methodology is applied to tackle this challenge and study these effects. For now, only the effects of  $Re_{\infty}$ ,  $\alpha$  and  $T_w/T_r$  are investigated in this paper.

# 2. Theory

### 2.1. Metric-based mesh adaptation

Mesh adaptation techniques aim at adapting the mesh based on a given metric, constructed from a prescribed sensor, in order to control the numerical errors, thus offering a higher fidelity and even a guarantee of the numerical solutions through mesh convergence. Moreover, it significantly alleviates the user time to reach a converged mesh and solution. In this subsection, all the formulas, concepts and notations are taken from the work of Loseille and Alauzet [4, 5, 6].

Based on the concepts of Riemannian metric space and continuous mesh theory, a control and a quantification of the edge sizes in any direction are possible. According to Alauzet and Olivier [6], given a metric tensor  $\mathcal{M}$  ( $d \times d$  symmetric positive definite matrix, where d is the domain dimension), various geometric quantities can be computed. For instance, in the Riemannian metric space, the length of a given edge **ab**, noted  $\ell_{\mathcal{M}}(\mathbf{ab})$ , is calculated as follows:

$$\ell_{\mathcal{M}}(\mathbf{ab}) = \int_0^1 \|\gamma'(t)\|_{\mathcal{M}} dt = \int_0^1 \sqrt{\mathbf{ab}^T \mathcal{M}(\mathbf{a} + t\mathbf{ab})\mathbf{ab}} dt, \tag{1}$$

using the straight line parameterization  $\gamma(t)=\mathbf{a}+t\mathbf{ab}$ , where  $t\in[0,1]$ . Besides, the volume of a given element K, noted  $|K|_{\mathcal{M}}$ , is given by

$$|K|_{\mathcal{M}} = \int_{K} \sqrt{\det(\mathcal{M}(\mathbf{x}))} \, dx.$$
 (2)

As introduced by George et al. [7], the main idea of metric-based mesh adaptation is to generate a unit mesh in the Riemannian metric space, meaning that each edge has a unit length  $(\forall e, \ell_{\mathcal{M}}(e) = 1)$ and each tetrahedron is regular  $(\forall K, |K|_{\mathcal{M}} = \sqrt{2}/12)$ . Ultimately, the resulting mesh in the Euclidean space will be anisotropic and adapted. This is precisely the reason why the Riemannian metric space

In the continuous mesh framework, the goal is to find the optimal continuous mesh  $M_{L^p}^{opt}$  that minimizes the continuous interpolation error in  $L^p$  norm, noted  $E_{L^p}$ . Thus, for a given computational domain  $\Omega$ , the goal is to find the optimal continuous mesh  $M_{L^p}^{opt}=(\mathcal{M}_{L^p}^{opt}(x))_{x\in\Omega}$  which minimizes the error  $E_{L^p}$ , where  $E_{L^p}$  is the error between a sensor u, which is a function of the conservative variables, and the continuous linear interpolate  $\pi_{\mathcal{M}}u$ . Besides, adding another constraint called the complexity  $\mathcal{C}$ , which enables the user to prescribe a desired number of vertices N in the mesh, the global optimization problem to be solved can be written as

$$E_{L^{p}}(M_{L^{p}}^{opt}) = \min_{M} E_{L^{p}}(M) = \min_{M} \|u - \pi_{\mathcal{M}}u\|_{L^{p}(\Omega)} = \min_{M} \left( \int_{\Omega} |u(x) - \pi_{\mathcal{M}}u(x)|^{p} dx \right)^{\frac{1}{p}}, \tag{3}$$

under the constraint

$$C(M) = \int_{\Omega} \sqrt{\det(\mathcal{M}(\mathbf{x}))} dx = \mathcal{N}.$$
 (4)

After derivation [4, 5, 6], the optimal continuous mesh  $M_{Lp}^{opt}$  can be obtained with the formula

$$\mathcal{M}_{L^p}^{opt} = \mathcal{N}^{\frac{2}{d}} \left( \int_{\Omega} (\det|\mathsf{H}_\mathsf{u}(\mathsf{x})|)^{\frac{p}{2p+d}} \mathsf{dx} \right)^{-\frac{2}{d}} (\det|\mathsf{H}_\mathsf{u}|)^{\frac{-1}{2p+d}} |\mathsf{H}_\mathsf{u}|. \tag{5}$$

Here,  $\mathcal{N}$  is the equivalent of the complexity  $\mathcal{C}$  in the discrete mesh framework and  $H_u$  is the hessian of the previously-mentioned sensor u. Ultimately,  $M_{L^p}^{opt}$  is unique and has optimal directions and ratios as the hessian's ones. In practice, the complexity  $\mathcal C$  and the norm p are both prescribed by the user. Besides, the optimal metric tensor  $\mathcal{M}_{L^p}^{opt}$  is obtained with the computation of the hessian of the sensor uwhich is usually the Mach number.

Copyright © 2025 by the author(s)

### 2.2. Local stability theory

After using the mesh adaptation based on the principles described in the previous section, flow solutions are obtained and their quality in the boundary layer region is assessed by means of stability analysis. It will be described next.

Stability theory relies on the introduction of a small perturbation on a steady base flow, defined as

$$q(\xi, \eta, \zeta, t) = \bar{q}(\xi, \eta, \zeta) + \epsilon q'(\xi, \eta, \zeta, t), \tag{6}$$

where q=(u,v,w,p,T). Whereas the flow undergoes fast variations in the wall normal direction, its streamwise and crosswise variations are slow compared to the perturbation variations. In the context of Local Stability Theory (LST), this is accounted for via the parallel flow assumption. As stated by Arnal and Casalis [8], this assumption indicates that the mean flow variation over a wavelength of the perturbation is negligible. Under the LST framework, non-linear effects are also neglected, leading to the following modal form of perturbation:

$$q'(\xi, \eta, \zeta, t) = \hat{q}(\eta)e^{i(\alpha\xi + \beta\zeta - \omega t)},\tag{7}$$

where the introduction of  $\beta$  is used to account for the azimuthal variations and to study oblique modes. Here,  $\omega$  is the angular frequency ( $\omega=2\pi f$ ) and the coefficients  $\alpha$  and  $\beta$  correspond respectively to the axial and transverse wavenumbers. Besides, the axial and transverse wavelengths can be obtained respectively with  $\lambda_{\xi}=2\pi/\alpha$  and  $\lambda_{\zeta}=2\pi/\beta$ . Furthermore, another parameter which is often introduced is the non-dimensional transverse wavenumber  $m_{\beta}$ , also noted n. For the specific case of a sphere-cone geometry,  $m_{\beta}=\beta\times R_{cone}(\xi)$  which results in the product of  $\beta$  and the local radius of the cone  $R_{cone}(\xi)$  at a given axial location  $\xi$  along the cone.

Introducing this formulation into the linearized Navier-Stokes equations leads to a linear generalized eigenvalue problem  $\mathcal{A}X=\alpha\mathcal{B}X$ . The vector X is composed of all  $\hat{q}$  and the matrices  $\mathcal{A}$  and  $\mathcal{B}$  both depend on the values of  $\omega$ ,  $\beta$  and the mean flow field. In practice, the numerical values of  $\omega$  and  $\beta$  are imposed, thus resulting in the calculation of the eigenvalue  $\alpha$  and the eigenfunctions in X. When the imaginary part of  $\alpha$ , also noted  $\alpha_i$ , is positive, the perturbation is damped along  $\xi$  but it is amplified when  $\alpha_i$  is negative.

From the LST results, various other parameters can be determined such as the ratio of local to initial amplitude  $A(\xi)/A_0$  or the local growth rate  $\sigma=-\alpha_i$  defined as

$$\sigma = \frac{1}{A} \frac{dA}{d\xi}.$$
 (8)

This growth rate may be used to compute the total growth of a given mode, called the N-factor and mathematically expressed as

$$N(\xi) = \int_{\xi_0}^{\xi} \sigma(s) \, ds. \tag{9}$$

Here,  $\xi_0$  is the location where the perturbation becomes unstable with an initial amplitude  $A_0$ .

## 3. Methodology

### 3.1. Mesh adaptation methodology

An iterative process is required to tackle the non-linear problem of mesh adaptation. As shown in Figure 1, the process starts with the generation of an initial mesh  $\mathcal{H}_0$  and an initial solution  $\mathcal{S}_0$  obtained from a CFD solver. Once calculated, a convergence criterion is evaluated. If the criterion is verified, the last mesh and solution are kept as final results. However, if it is not satisfied, the mesh adaptation loop starts or continues. First, based on a computed error estimate metric, the mesh is adapted by a remesher. In this work, the mesh adaptation is performed with the open-source software refine [9, 10] to take advantage of its parallel/partitioned capability where the loop between the CFD solver and the remesher is automatically handled with an in-house mesh adaptation tool.

Then, the previously-obtained solution is interpolated on the newly-obtained adapted mesh. Finally, the new mesh and solution are put as new input of the CFD solver and the loop continues until the user-defined convergence criterion is verified. In this work, approximately 50 boundary layer profiles are chosen on the cone and various first and second derivatives of the boundary layer profiles  $(u, \rho, \mu)$  are plotted before each mesh adaptation. When the convergence of these derivatives are deemed sufficient, the loop stops, the same or another set of boundary layer profiles are extracted and stability analyses are performed for these profiles.

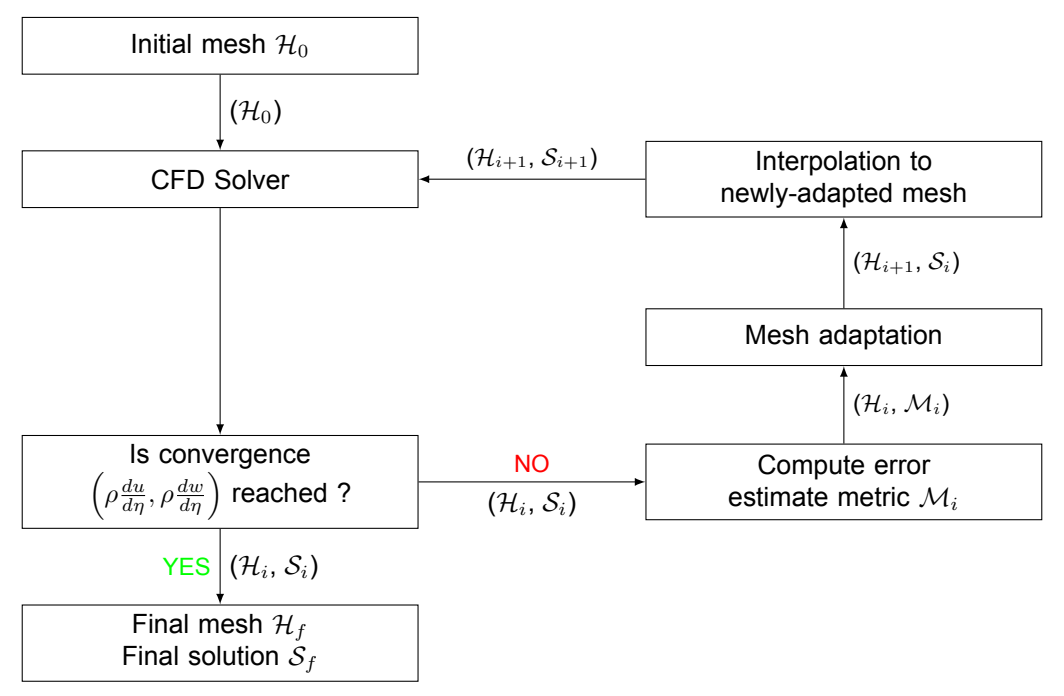


Fig 1. Block diagram of the mesh adaptation methodology.

### 3.2. Geometry and CFD solver methodology

In this work, only sphere-cone geometries have been investigated. The geometry is thus defined by the nosetip radius  $R_N$ , the cone semi-angle  $\theta_c$  and the cone length  $L_c$ . In the following sections, two other coordinates noted  $\xi$  and  $\phi$  are introduced where  $\xi$  is the longitudinal abscissa along the cone and  $\phi$  is the azimuthal angle from the windward symmetry plane at a given axial location  $\xi$ , as shown in Figure 2.

To perform the CFD calculations, the solver SoNICS (ONERA-Safran property) [11] is used to take advantage of its numerical robustness for meshes composed of highly anisotropic tetrahedra. In particular, the V4 vertex-centered finite volume scheme, initially developed by Dervieux [12], Rostand and Stoufflet [13] has been used in this work.

The control volumes are built around mesh vertices following the median cell approach to define the dual cells. To compute the convective fluxes, a HLLC-Riemann solver is used and, for the viscous fluxes, a five-point stencil approach is chosen. Moreover, time integration is performed using an implicit backward Euler method, where the implicit procedure is a SSOR method.

Regarding the boundary conditions, supersonic inflow and outflow conditions are imposed in the inlet and outlet, respectively. Symmetry boundary conditions are imposed for the leeward and windward symmetry planes. Finally, an isothermal no-slip boundary condition was imposed on the sphere and the cone.

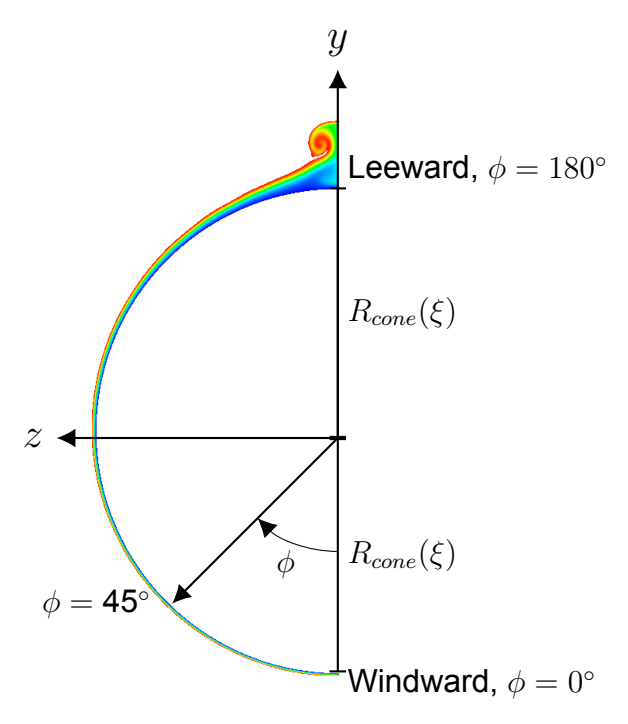


**Fig 2.** Definition of the azimuthal angle  $\phi$  around the cone at a given axial location  $\xi$ .

## 4. Validation of the methodology

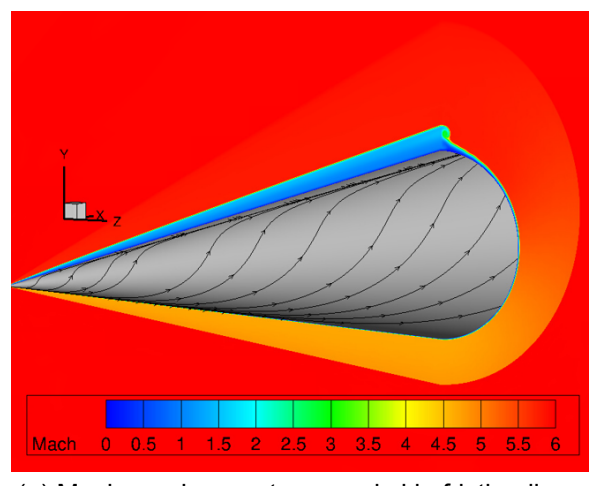
#### 4.1. Circular sharp cone

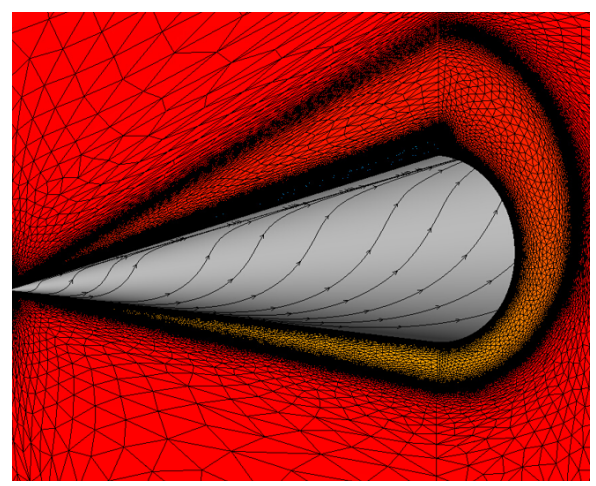
For validation purposes, our results will be compared against the recent ones in Liu *et al.* [14], focusing only on stability diagrams. Table 1 indicates the flow conditions for the case taken from Liu *et al.* [14]. The geometry is a sharp cone with a nosetip radius of  $R_N=0.05$  mm, a semi-angle of  $\theta_c=7^\circ$  and a cone length of  $L_c=0.4$  m. In the rest of the paper, the term 'sharp' will be used to characterize a cone where the nosetip radius is extremely small compared to the cone length.

**Table 1.** Flow conditions for the sharp cone.

$M_{\infty}$	$Re_{\infty}$ [/m]	$T_{\infty}$ [K]	<i>AoA</i> [°]	$T_w$ [K]
6.0	$10.0 \times 10^{6}$	48.00	6.0	300.0

First, the Mach number contours can be displayed to observe the detached shock and the boundary layer, respectively. As shown in Figure 3, some known flow features are observed: a streamwise vortex, a movement of the flow towards the leeward plane induced by the azimuthal pressure gradient and a detached shock. It is clear from Figure 3 that the tetrahedral mesh elements are extremely well suited to capture the detached shock.



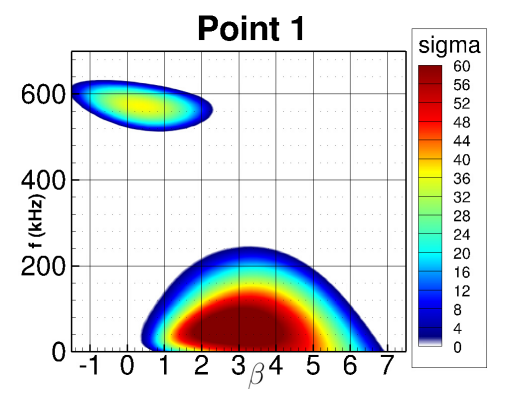


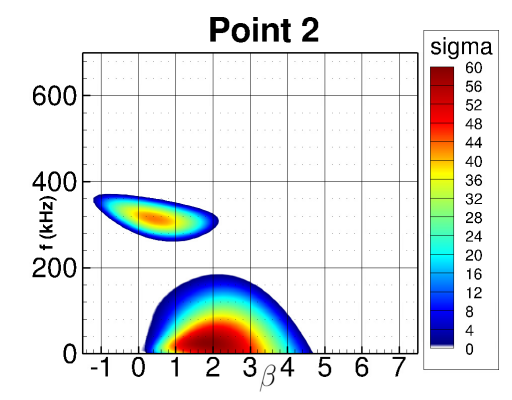
(a) Mach number contours and skin friction lines

(b) Mach number contours and adapted mesh

Fig 3. Mach number contours, skin friction lines and the associated mesh

To validate the methodology with the state of the art in base flow computation and LST, stability diagrams at two locations on the cone are plotted in Figure 4. The boundary layer profiles are taken along a streamline drawn in [14] at  $(\xi,\phi)=(0.102~\text{m},61^\circ)$  and  $(\xi,\phi)=(0.190~\text{m},90^\circ)$  which are respectively called Point 1 and Point 2 in Figure 4. For both boundary layer profiles, a high-frequency second Mack mode and a low-frequency crossflow instability are observed. Besides, the numerical values of  $\sigma$ ,  $\beta$  and the frequency in the center of the lobes are in agreement with the results of Liu *et al.* [14]. For instance, for the profile at  $(\xi,\phi)=(0.190~\text{m},90^\circ)$ , values of  $\beta\approx0.5~\text{[/mm]}$ ,  $\sigma\approx42~\text{[/m]}$  and  $f\approx330~\text{[kHz]}$  are obtained for the second Mack mode and  $\beta\approx2.0~\text{[/mm]}$ ,  $\sigma\approx60~\text{[/m]}$  and  $f\approx30~\text{[kHz]}$  for the crossflow instability.





(a) Results at  $\phi$  = 61 [°] from current methodology (b) R



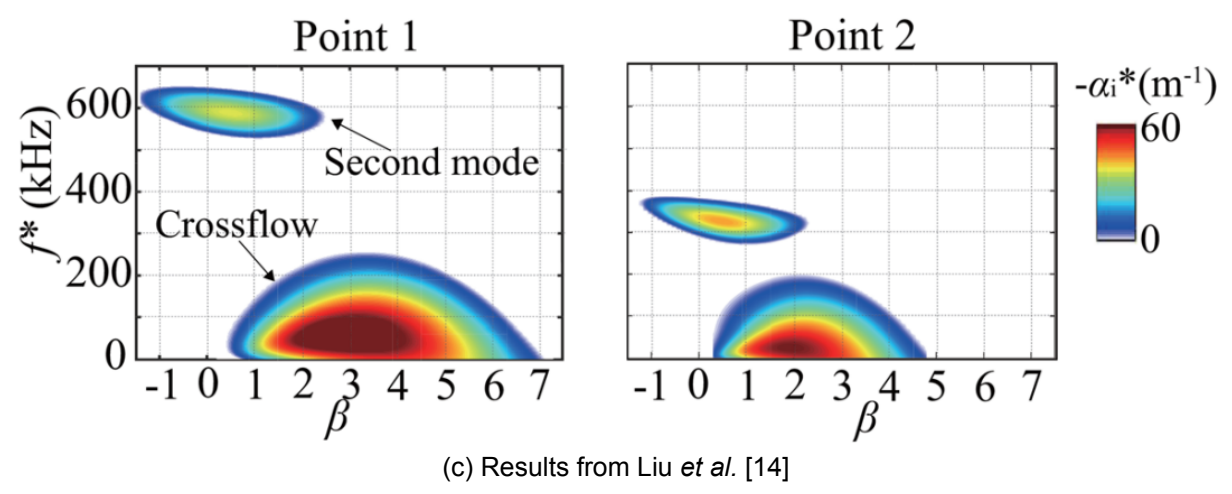


**Fig 4.** Growth rate  $\sigma$  [/m] in terms of the frequency f [kHz] and the azimuthal wavenumber  $\beta$  [/mm].

### 4.2. Elliptic blunt cone (HIFIRE-5)

In this subsection, our results will be compared against those presented by Li *et al.* [15] on the HIFIRE-5 geometry (see Figure 5), as well as against some experimental data from Borg *et al.* [16] under quiet flow at zero angle of attack. The flow conditions are indicated in Table 2. The first flow condition was used to validate the profiles of  $\rho \frac{du}{d\eta}$  presented in Figure 6 whereas the second flow condition was used to validate the 1D fluctuations and N-factors, respectively shown in Figure 7 and in Figure 8.

Although this is a zero angle of attack case, there is still a movement of the fluid from the major axis meridian (attachment line) towards the minor axis meridian due to the azimuthal pressure gradient created by the curvature of the bow shock, as shown in Figure 5(d) using pressure contours. This is due to the fact that the elliptic section of the geometry induces a shock located at a wall-normal distance that differs for each azimuthal angle  $\phi$  around the cone and thus creates a non-zero azimuthal pressure gradient that drives the flow towards the minor axis meridian. Close to the latter, the flow lifts up and a vortical structure forms similarly to the inclined circular cone case, as shown in Figure 5(c).

Table 2. Flow conditions for the validation on the HIFIRE-5 geometry

$\overline{M}$	$_{\infty}$ $I$	$Re_{\infty}$ [/m]	$ ho_{\infty}$ [kg/m $^3$ ]	$T_{\infty}$ [K]	$P_{\infty}$ [kPa]	$U_{\infty}$ [m/s]	$T_w$ [K]
6.	0 9.	$843 \times 10^{6}$	0.04034	52.8	0.611	873.92	300
6.	0 8.	$275 \times 10^6$	0.03121	49.9	0.477	849.84	300

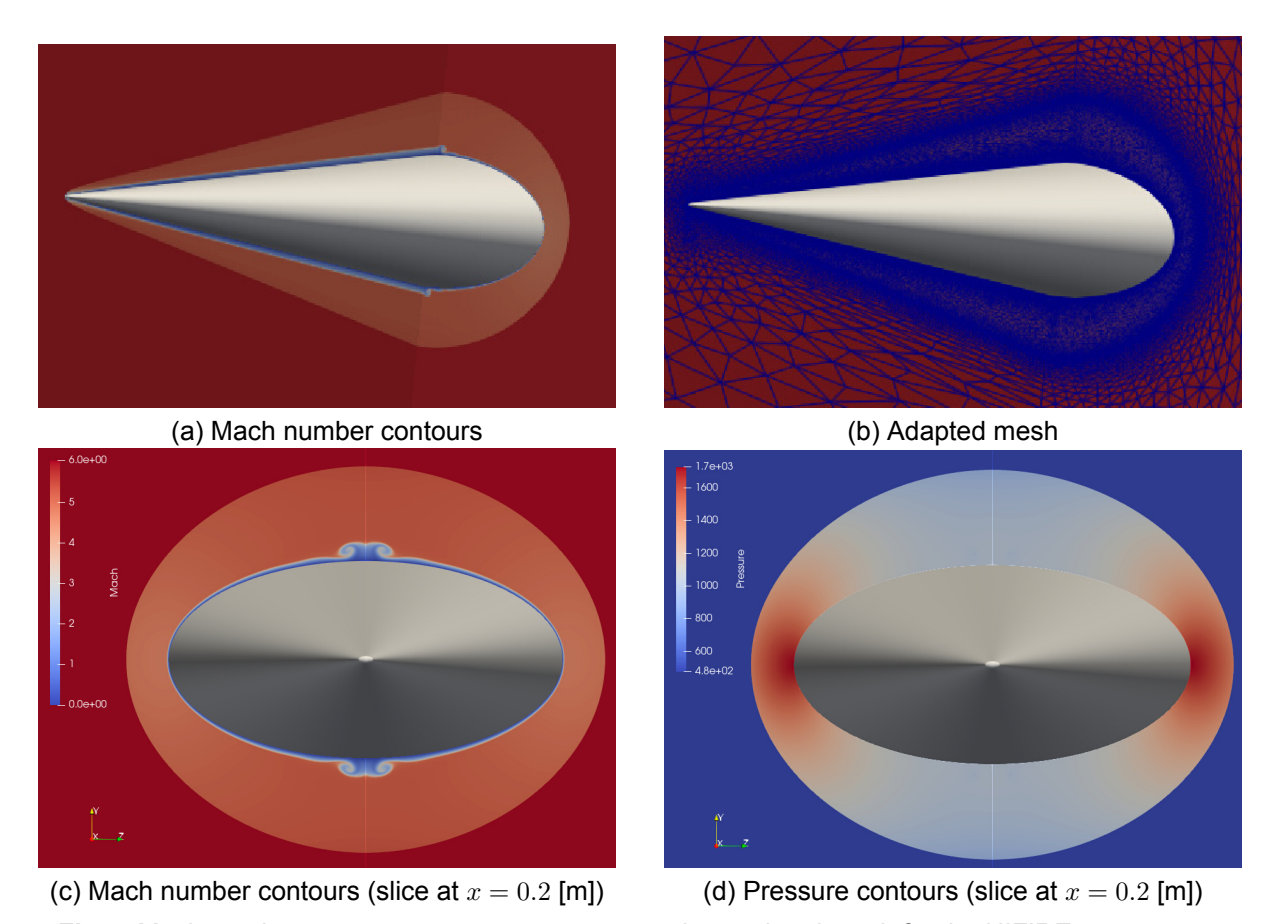
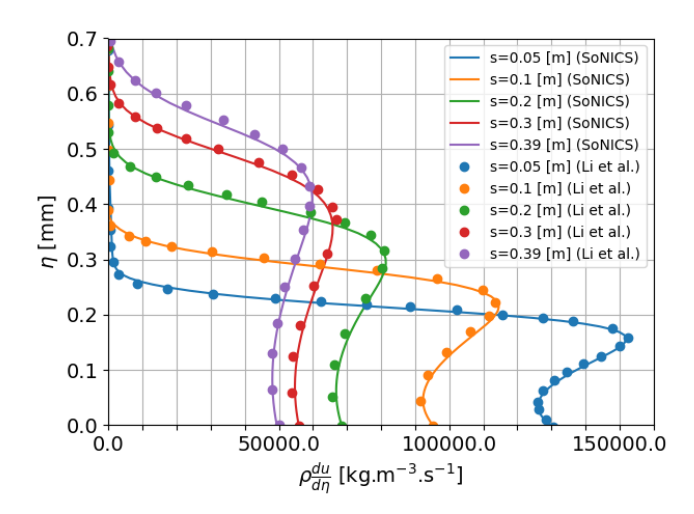


Fig 5. Mach number contours, pressure contours and associated mesh for the HIFIRE-5 geometry.

Regarding the validation of the methodology on this geometry, profiles of  $\rho \frac{du}{d\eta}$  have been plotted at various locations along the attachment line. As shown in Figure 6, it has been found that the current methodology was able to reproduce the profiles from Li *et al.* [15] with negligible discrepancies.

Moreover, 1D fluctuations and N-factors for both the crossflow instability and the second Mack mode at a specific location around the cone have been extracted. It corresponds to the location where a Kulite sensor (sensor 1) was placed by Borg et al. [16] at x=0.3125 [m] and z=0.0371 [m]. As shown in Figure 7, the wall-normal distribution of |u'|, |T'| and |p'| are in very good agreement with the results from Li et al. [15]. It has been observed that the pressure fluctuation is not maximum at the wall but at a wall-normal distance located at the generalized inflexion point (GIP) for the crossflow velocity profile. This is probably the reason why the small peak frequency of the crossflow mode is often difficult to measure experimentally, considering that mostly wall pressure sensors are used. Moreover, as shown in the N-factor distribution in Figure 8, the most unstable frequency predicted numerically for the crossflow instability matches the experimental measurements, thus highlighting the validation of the methodology but also of the domain of validity of the local stability theory. From the numerical results, it is fair to say that a good agreement has also been found for the second Mack mode (N pprox 2) and the crossflow instability ( $N \approx 11.5-12$ ). It is fair to mention that a slight difference has been obtained for the maximum N-factor at f = 40 [kHz] compared to the results of Li *et al.* [15]. It could be hypothesized that this difference of  $\Delta N \approx 0.5$  could originate from slightly different locations of the boundary layer profiles along the streamline but also the number of azimuthal wavenumbers  $\beta$  (or m) used in the calculations. Besides, it could also come from the fact that Li et al. [15] have used QPWC to compute the growth rates, whereas only LST was used in the current methodology. QPWC stands for Quasi-Parallel With Curvature, which is LST including the curvature effects.



**Fig 6.** Comparison between the current methodology and the results from Li *et al.* [15] of the profiles of  $\rho \frac{du}{dn}$  at various locations along the attachment line for the HIFIRE-5 geometry

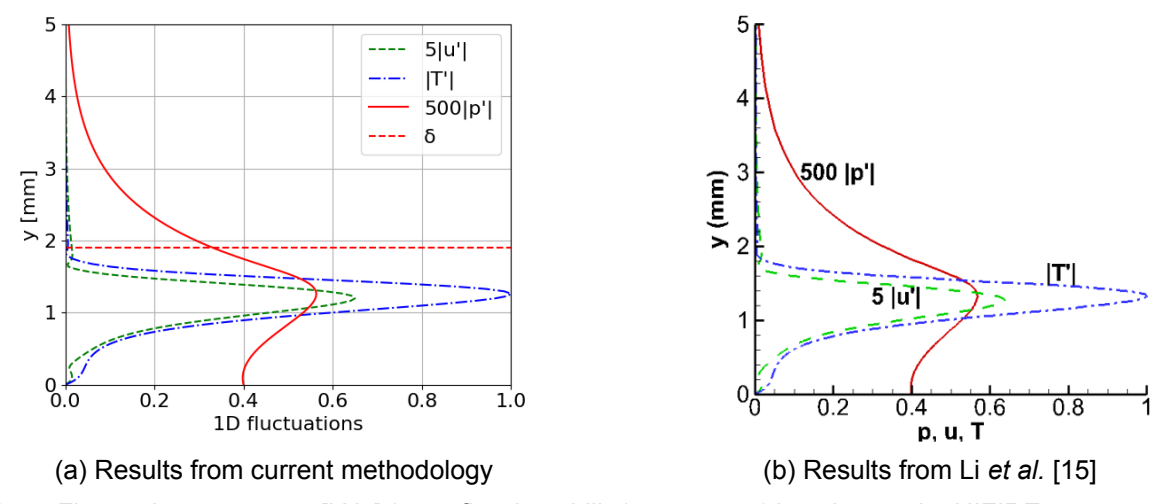


Fig 7. Fluctuations at f = 40 [kHz] (crossflow instability) at sensor 1 location on the HIFIRE-5 geometry

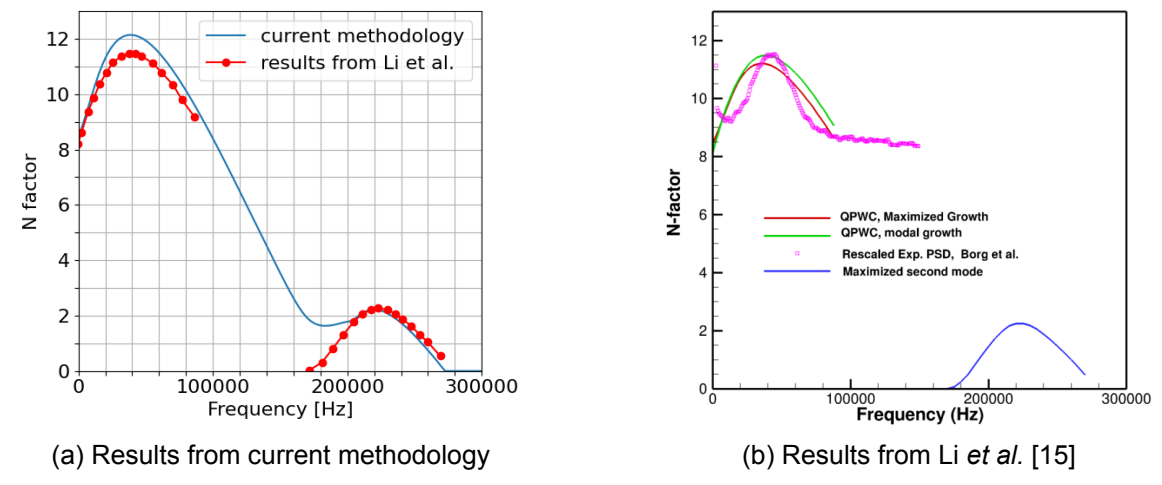


Fig 8. N-factor at sensor 1 location and comparison with experimental data for the HIFIRE-5 geometry

### 5. Parametric study

In this section, a parametric study on the parameters  $T_w/T_r$ ,  $Re_\infty$  and  $\alpha$  is performed for an inclined circular sharp cone with  $R_N=0.05$  mm,  $\theta_c=7^\circ$  and  $L_c=0.5$  m.

#### 5.1. Wall temperature effects

In this subsection, the effect of the parameter  $T_w/T_0$  or, more precisely, of the ratio  $T_w/T_r$  where the recovery temperature can be calculated with the formula

$$T_r = T_{\infty} \left( 1 + \frac{\gamma - 1}{2} \sqrt{\Pr} M_{\infty}^2 \right), \tag{10}$$

where  $\Pr=0.72$  and  $T_r=369.69$  [K], is studied in the range including typical values for conventional wind tunnels. As presented in Table 3, the freestream flow conditions are kept constant and only the wall temperature is changed from  $T_w=100$  [K] ( $T_w/T_r=0.2705$ ) to  $T_w=388$  [K] ( $T_w/T_r=1.0495$ ). The angle of attack has been fixed at a sufficiently high incidence of  $\alpha=3^\circ$  to illustrate the effect of the ratio  $T_w/T_r$  on the crossflow instability.

**Table 3.** Flow conditions considered for the study on the effects of the wall temperature ratio  $T_w/T_r$ .

$M_{\infty}$	$Re_{\infty}$ [/m]	AoA [°]	$T_w$ [K]	$T_{\infty}$ [K]	$T_{0,\infty}$ [K]	$T_w/T_0$	$T_w/T_r$
6.0	$10.0\times10^6$	3.0	100.0	52.00	426.4	0.2345	0.2705
6.0	$10.0 \times 10^{6}$	3.0	200.0	52.00	426.4	0.4690	0.5410
6.0	$10.0 \times 10^{6}$	3.0	300.0	52.00	426.4	0.7036	0.8115
6.0	$10.0 \times 10^{6}$	3.0	388.0	52.00	426.4	0.9099	1.0495

To highlight the effect of this parameter, boundary layer profiles are taken at the same axial location along the cone but at various azimuthal angles  $\phi$ , ranging from  $\phi=0^\circ$  to  $\phi=140^\circ$  with a spacing of  $20^\circ$ , and stability analyses are performed for the first and second Mack modes but also for the crossflow instability. For the sake of conciseness, only the stability results at x=0.2 [m] are presented. Besides, it is worth mentioning here that, considering that the edge quantities vary for each value of  $\phi$  as shown in Figure 9, the results cannot technically be compared for a given value of  $T_w/T_r$ . However, not only is it useful to get an order of magnitude of this effect, but it is reasonable to compare the results at fixed values of  $(x,\phi)$  for various  $T_w/T_r$  values because the values of  $M_e$ ,  $T_e$  and  $Re_e=\rho_e U_e/\mu_e$  are roughly constant. Indeed, as shown in Figure 9, the values of  $M_e$ ,  $T_e$ ,  $U_e$  and  $\mu_e$  vary less than 3% and consequently this variation can be neglected. Nevertheless, as shown in Figure 9, it is clear that increasing the ratio  $T_w/T_r$  leads to an increased displacement effect that might slightly displace the shock location, thus possibly explaining the slight variation of the edge quantities when the wall temperature is changed. Indeed, it has been found at  $\phi=80^\circ$  that  $\delta_1=0.4$  [mm] for  $T_w/T_r=0.2705$  and  $\delta_1=0.7$  [mm] for  $T_w/T_r=0.8115$ , thus quantitatively proving that this increased displacement effect is far from negligible.

Then, the non-dimensional temperature  $T/T_r$  profiles are displayed in Figure 10. It has been observed that the gradient at the wall (wall heat flux) at a given value of  $\phi$  decreases until  $T_w/T_r=1.0495$  where it is almost zero due to the fact that the wall is almost adiabatic. Besides, at a given value of  $T_w/T_r$ , it can be seen that it decreases because of the thickening of the boundary layer when  $\phi$  increases. From the temperature profiles, it is also clear that the viscosity is also significantly affected by the values of  $T_w/T_r$ . Moreover, as presented in Figure 11, the values of  $(\rho \, du/d\eta)|_{\eta=0}$  differ significantly when the ratio  $T_w/T_r$  is increased, with values ranging at  $\phi=0^\circ$  from  $(\rho \, du/d\eta)|_{\eta=0}\approx 175000$  [kg.m $^{-3}$ .s $^{-1}$ ] at  $T_w/T_r=0.2705$  to  $(\rho \, du/d\eta)|_{\eta=0}\approx 17000$  [kg.m $^{-3}$ .s $^{-1}$ ] at  $T_w/T_r=1.0495$ . This highlights the impact specifically at the wall that the ratio  $T_w/T_r$  can have on the boundary layer profiles. Considering that  $T_w/T_r \leq 0.3$  and  $T_w/T_r \approx 0.8$  are respectively representative of flight and wind tunnel flow conditions, it is clear that a wide range of  $T_w/T_r$  values must be taken into account in transition modeling for a broad scope of applications.

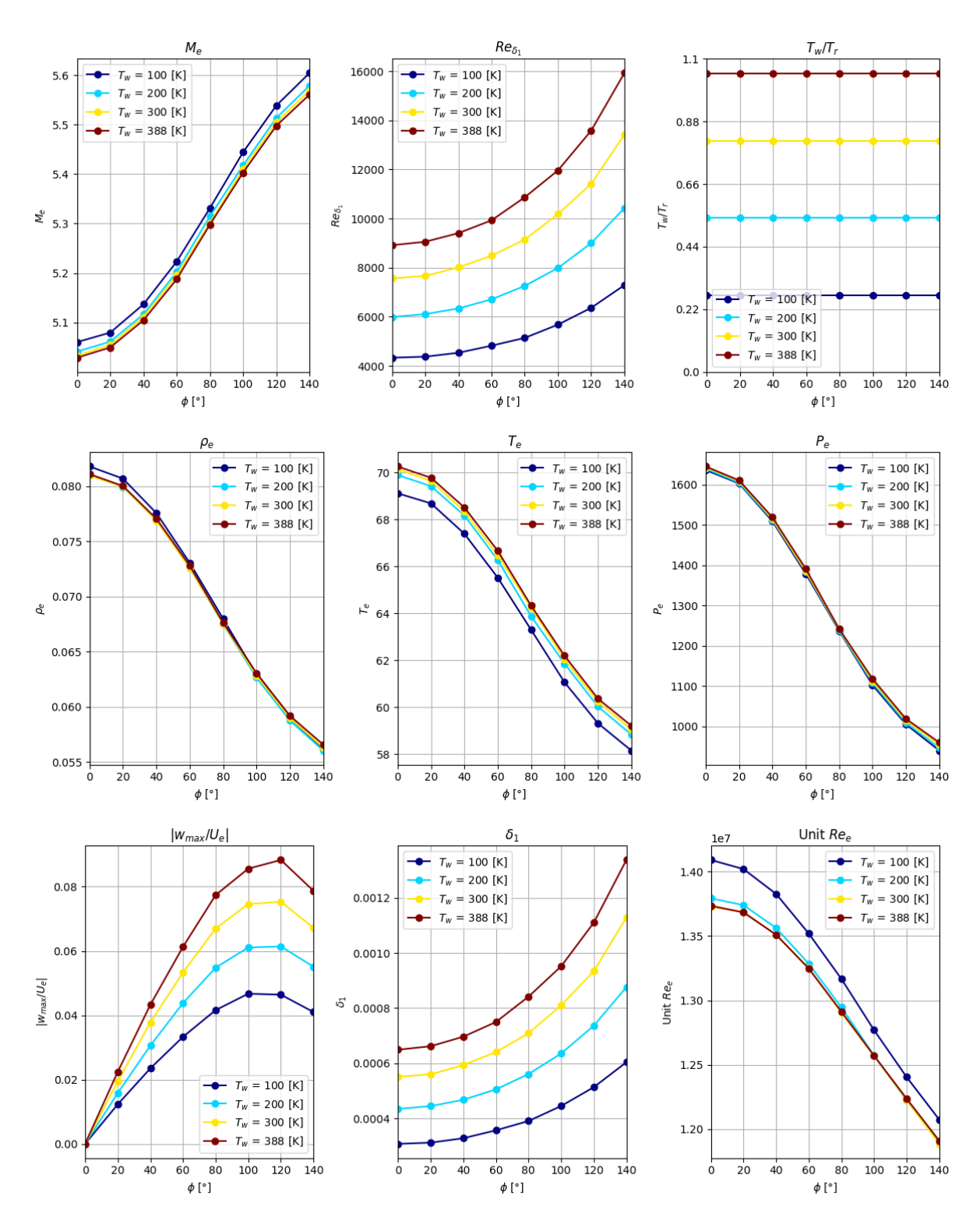


**Fig 9.** Wall temperature (or  $T_w/T_r$ ) effects on the edge quantities  $M_e$ ,  $Re_{\delta_1}$ ,  $T_w/T_r$ ,  $\rho_e$ ,  $T_e$ ,  $P_e$ ,  $|w_{max}/U_e|$ ,  $\delta_1$  and  $Re_{e,unit}$  for various azimuthal angles  $\phi$  around the cone at x=0.2 [m].

Regarding the three-dimensional effects, the previous remark still holds when looking at the  $ho rac{dw}{d\eta}$  profiles plotted in Figure 11. Indeed, the values of  $(\rho\,dw/d\eta)|_{\eta=0}$  varied tremendously, ranging at  $\phi=80^\circ$  from  $(\rho\,dw/d\eta)|_{\eta=0} pprox -15000$  [kg.m $^{-3}$ .s $^{-1}$ ] at  $T_w/T_r = 0.2705$  to  $(\rho\,dw/d\eta)|_{\eta=0} pprox -3000$  [kg.m $^{-3}$ .s $^{-1}$ ] at  $T_w/T_r = 1.0495$ . Besides, although the boundary layer thickness increases significantly when  $T_w/T_r$ increases, the variation of  $(\rho dw/d\eta)|_{\eta=GIP_m}$  is surprisingly small with a minor increase. Moreover, as presented in Figure 12, it has been found that the  $T_w/T_r$  ratio influences significantly the values of  $|w_{max}/U_e|$  ranging at  $\phi=120^\circ$  from  $|w_{max}/U_e|\approx 4.7\%$  at  $T_w/T_r=0.2705$  to  $|w_{max}/U_e|\approx 8.7\%$ at  $T_w/T_r=1.0495$  for the chosen freestream flow conditions. This shows that the ratio  $T_w/T_r$  does not simply affect the temperature and viscosity profiles, it also increases the three-dimensionality of the flow. It is here worth noting that this correlates with the observations of Wang et al. [17] where increased values of  $u_{c,max}$  (different notation but same definition as  $|w_{max}/U_e|$ ) were observed when the wall temperature was increased from  $T_w=150$  [K] to  $T_w=450$  [K] for a blunt cone ( $R_N=1$  [mm]) at  $\alpha=5^{\circ}$ . Besides, it had been shown by the authors of [17] that the value of  $|w_{max}/U_e|$  doubled between the lowest and highest wall temperature, which is an increase of the same order of magnitude as in this present work.

Theoretically, the shape of the  $ho rac{du}{d\eta}$  and  $ho rac{dw}{d\eta}$  profiles is indicative of the presence or absence of certain instability waves. Indeed, the first Mack mode and the crossflow instability being of inflectional nature, they can only exist if a generalized inflexion point exists, respectively on the longitudinal and crossflow velocity component, defined as follows:

$$\frac{d}{d\eta} \left( \rho \frac{du}{d\eta} \right) = 0 \tag{11}$$

$$\frac{d}{d\eta} \left( \rho \frac{du}{d\eta} \right) = 0 \tag{11}$$

$$\frac{d}{d\eta} \left( \rho \frac{dw}{d\eta} \right) = 0. \tag{12}$$

Equivalently, they cannot exist if the profiles of  $\rho \frac{du}{d\eta}$  and  $\rho \frac{dw}{d\eta}$  do not admit local extrema respectively. Consequently, as shown in Figure 11 for the  $\rho \frac{du}{d\eta}$  profiles, the first Mack mode is not expected to be unstable for  $T_w/T_r=0.2705$  but is expected to be unstable for  $T_w/T_r=0.5410$ . However, as shown in Figure 11, the crossflow instability is always expected to be unstable because the profiles of  $\rho \frac{dw}{dn}$  always admit a local extrema, except at  $\phi = 0^{\circ}$  because the crossflow velocity must be zero in the symmetry plane. This has been verified using the growth rate variation in terms of the frequency presented in Figure 13 where the first Mack mode is stable at  $\phi=0^\circ$  for the  $T_w/T_r=0.2705$  wall condition yet becomes unstable for  $T_w/T_r=0.5410$  at the same location. Besides, it has been found that both the first Mack mode and the crossflow instability are destabilized by an increase in  $T_w/T_r$  and that both the most unstable frequency and the range of unstable frequencies increased with  $T_w/T_r$ . Considering that the only boundary layer parameters changing at a given  $\phi$  location when the wall temperature is increased are  $T_w/T_r$ ,  $Re_{\delta_1}$  and  $|w_{max}/U_e|$  (see Figure 9), it is thus worth noting that these frequencies must depend on these specific parameters. However, since the ratio  $T_w/T_r$  is only the driver for variations of  $Re_{\delta_1}$  and  $|w_{max}/U_e|$ , the unstable frequencies can be expressed in terms of those quantities modified by  $T_w/T_r$ , amongst which  $Re_{\delta_1}$  and  $|w_{max}/U_e|$  should be included.

Regarding the second Mack mode, Figure 13 clearly highlights that it is stabilized by an increase in  $T_w/T_r$  where the crossflow instability becomes even dominant for some values of  $\phi$  at  $T_w/T_r = 1.0495$ . Moreover, as the boundary layer thickens, the most unstable frequency of the second Mack mode has been found to decrease notably, ranging from 240-600 [kHz] for  $T_w/T_r=0.2705$  to 170-470 [kHz] for  $T_w/T_r = 1.0495$ . The observed trend is consistent with the widely used estimate for the second Mack mode frequency given by:

$$f_{mode2} pprox rac{U_e}{2\delta}.$$
 (13)

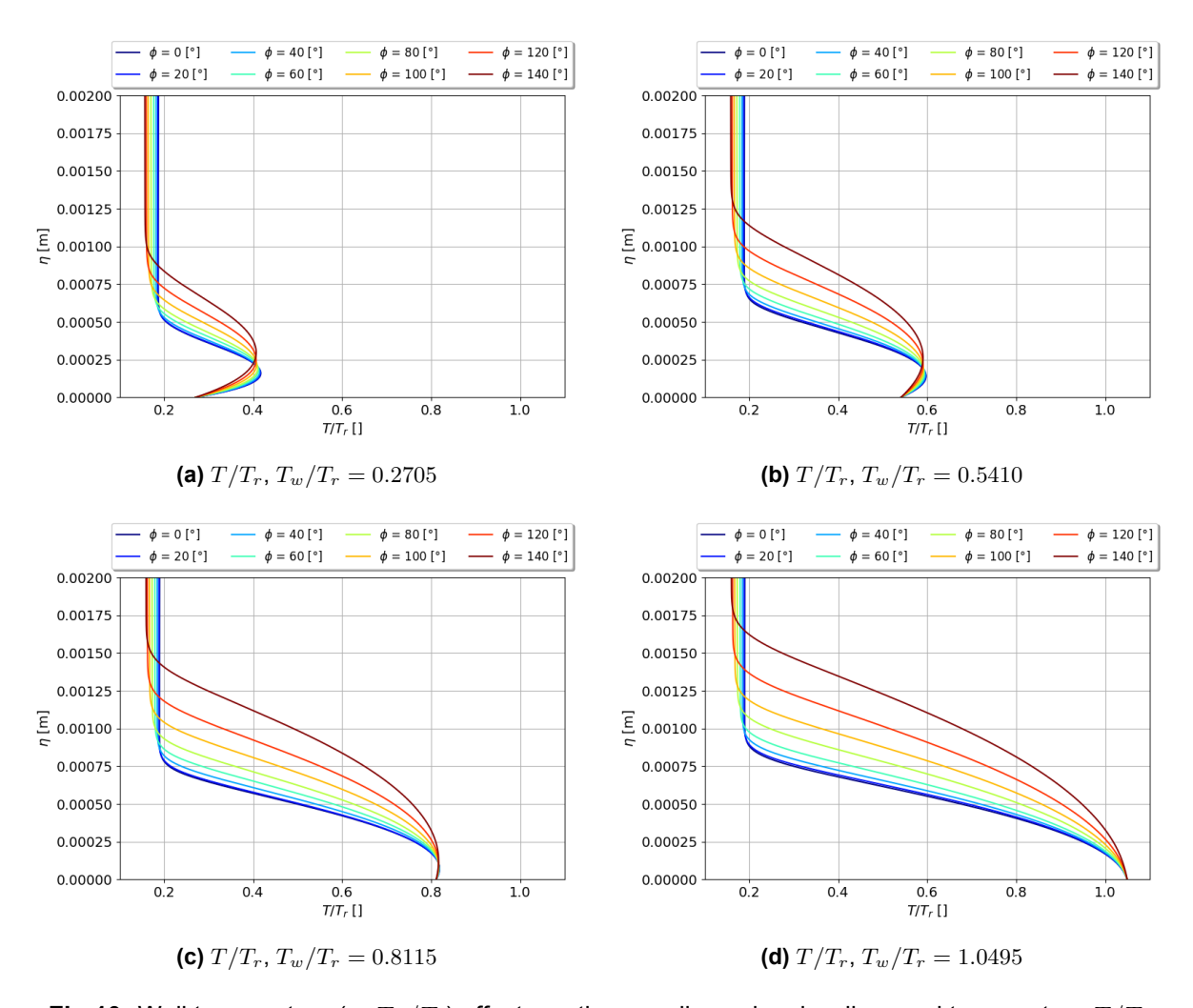


Fig 10. Wall temperature (or  $T_w/T_r$ ) effects on the non-dimensional wall-normal temperature  $T/T_r$  profiles at x=0.2 [m] for various azimuthal angles  $\phi$  around the cone.

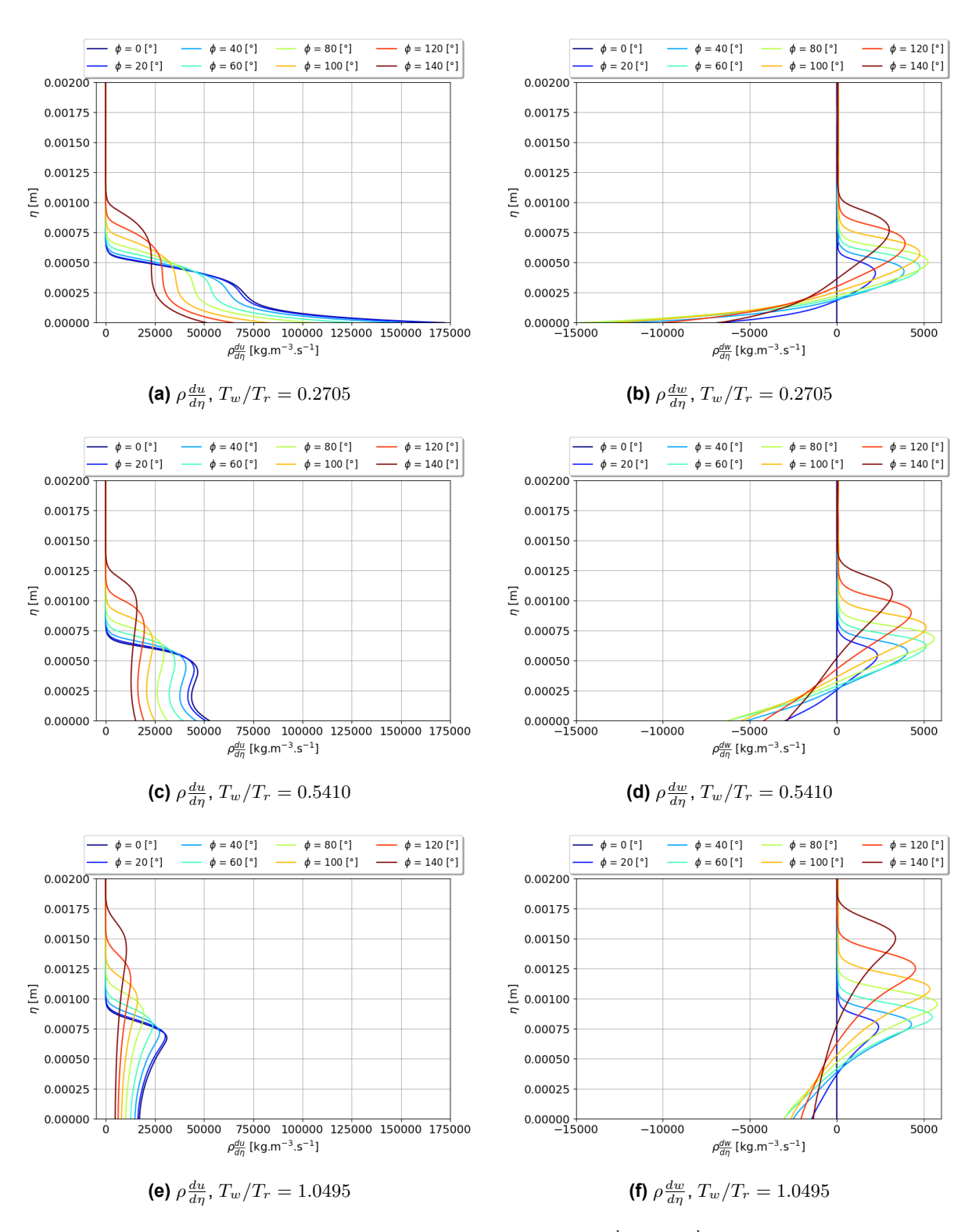


Fig 11. Wall temperature (or  $T_w/T_r$ ) effects on the profiles of  $\rho \frac{du}{d\eta}$  and  $\rho \frac{dw}{d\eta}$  at x=0.2 [m] for various azimuthal angles  $\phi$  around the cone.

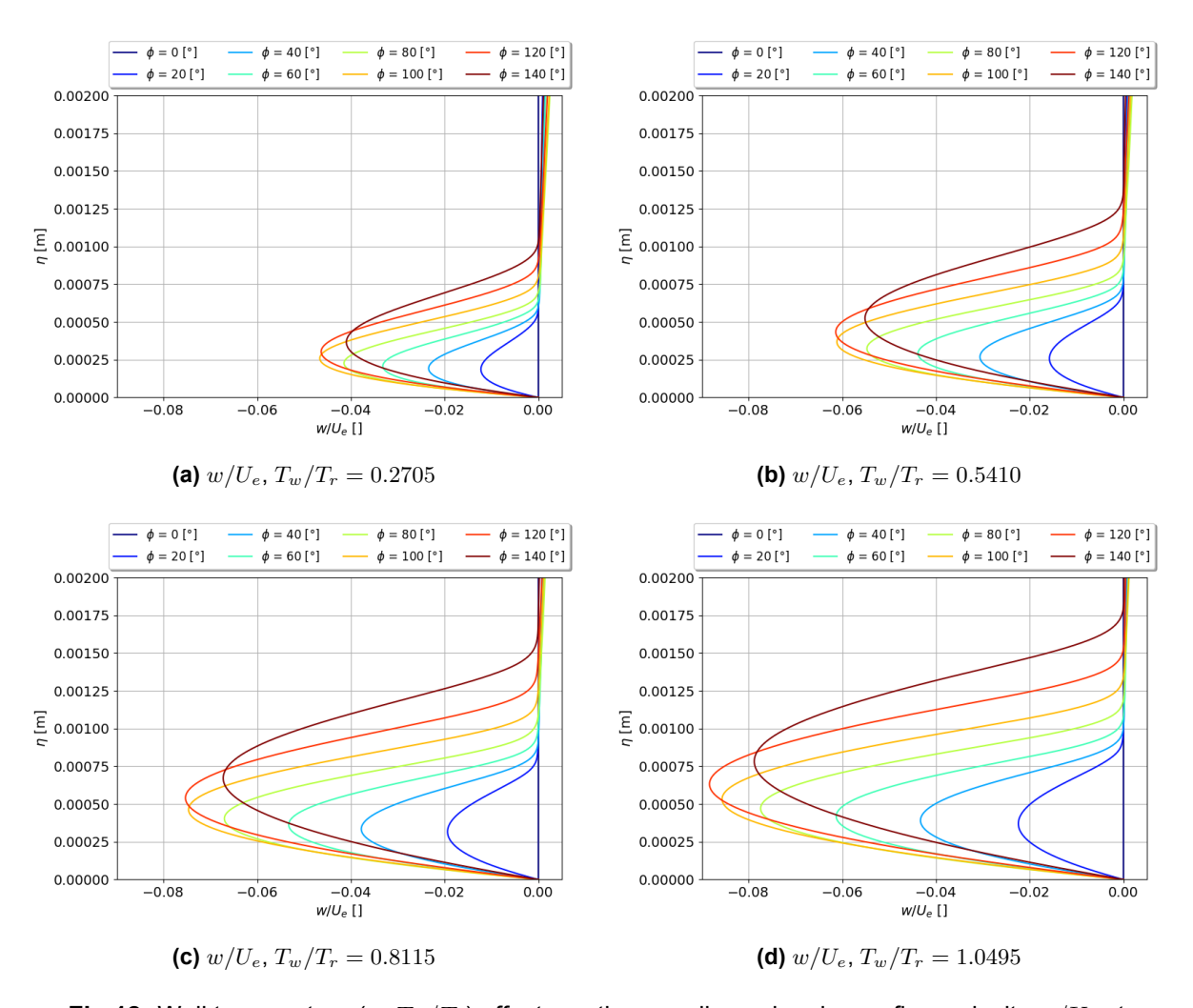


Fig 12. Wall temperature (or  $T_w/T_r$ ) effects on the non-dimensional crossflow velocity  $w/U_e$  at x=0.2 [m] for various azimuthal angles  $\phi$  around the cone.

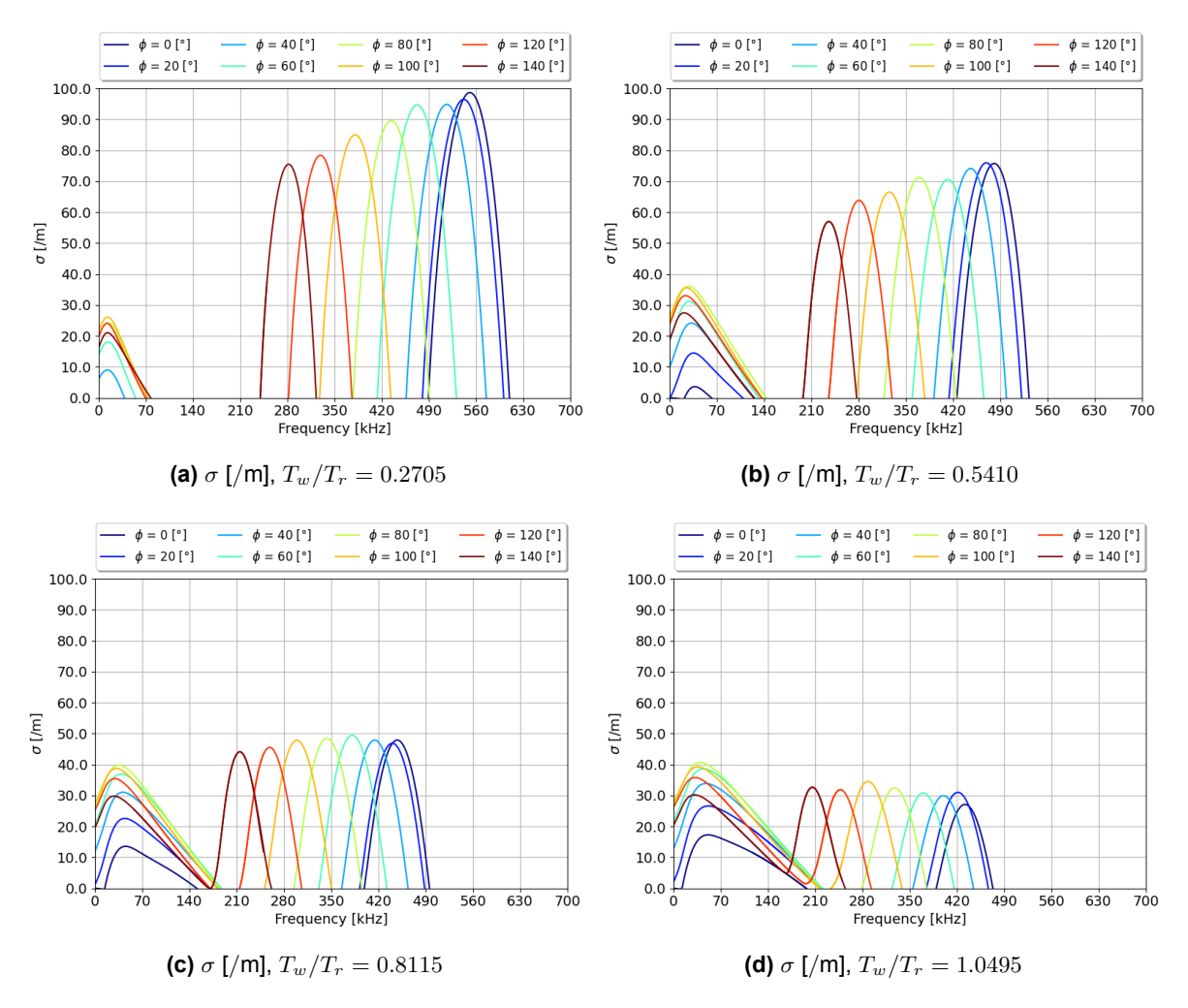


Fig 13. Wall temperature (or  $T_w/T_r$ ) effects on the Mack modes and crossflow instability growth rates and frequencies at x = 0.2 [m] for various azimuthal angles  $\phi$  around the cone.

HiSST-2025-174 Copyright © 2025 by the author(s)

Page | 17

#### 5.2. Reynolds number effect

In this subsection, the effect of the freestream unit Reynolds number is studied. As shown in Table 4, this parameter is being varied from  $Re_{\infty}=8.0\times10^6$  [/m] to  $Re_{\infty}=14.0\times10^6$  [/m]. In order to study the effect of this parameter on the crossflow instability, the angle of attack is fixed at  $\alpha=3^{\circ}$ . Besides, considering the observation from the wall temperature effects, the temperature ratio is fixed at  $T_w/T_r=0.8115$  to make sure that the three modes are unstable.

$M_{\infty}$	$Re_{\infty}$ [/m]	<i>AoA</i> [°]	$T_w$ [K]	$T_{\infty}$ [K]	$T_{0,\infty}$ [K]	$T_w/T_r$
6.0	$8.0 \times 10^6$	3.0	300.0	52.00	426.4	0.8115
6.0	$10.0 \times 10^{6}$	3.0	300.0	52.00	426.4	0.8115
6.0	$12.0 \times 10^{6}$	3.0	300.0	52.00	426.4	0.8115
6.0	$14.0 \times 10^{6}$	3.0	300.0	52.00	426.4	0.8115

**Table 4.** Flow conditions considered for the study on the unit Reynolds number effects.

The non-dimensional longitudinal velocity  $u/U_e$  profiles are presented in Figure 15. It has been observed that the Reynolds number induces a lower boundary layer thickness for all values of  $\phi$ . Moreover, as shown in Figure 15 and contrary to the wall temperature ratio  $T_w/T_r$  effects, the freestream Reynolds number does not affect the three-dimensionality of the flow. Indeed, at a given  $\phi$  location, the value of  $|w_{max}/U_e|$  is completely unchanged when increasing the Reynolds number. However, as shown in Figure 16, the values of  $\rho \frac{du}{d\eta}$  and  $\rho \frac{dw}{d\eta}$  have notably changed with the increase in Reynolds number. Indeed, the values of  $(\rho \, dw/d\eta)|_{\eta=0}$  at  $\phi=80^\circ$  went from  $(\rho \, dw/d\eta)|_{\eta=0}=-3000$  [kg.m $^{-3}$ .s $^{-1}$ ] at  $Re_\infty=8.0\times10^6$  [/m] to  $(\rho \, dw/d\eta)|_{\eta=GIP_w}$  at  $\phi=80^\circ$  that went from  $(\rho \, dw/d\eta)|_{\eta=GIP_w}=4000$  [kg.m $^{-3}$ .s $^{-1}$ ] at  $Re_\infty=8.0\times10^6$  [/m] to  $(\rho \, dw/d\eta)|_{\eta=GIP_w}=9100$  [kg.m $^{-3}$ .s $^{-1}$ ] at  $Re_\infty=14.00\times10^6$  [/m]. This shows that the Reynolds number has a strong effect on the profiles in the near-wall region but also in the outer part of the boundary layer.

Regarding the stability results, Figure 17 sheds light on the variation of the growth rate in terms of the frequency for all the chosen Reynolds numbers and the selected  $\phi$  locations. It appears that the Reynolds number has a destabilizing effect on all the modes: the first Mack mode at  $\phi=0^\circ$ , the crossflow instability at  $\phi>0^\circ$  and the high-frequency second Mack mode. For instance, it has quantitatively been found for the first Mack mode at  $\phi=0^\circ$  that  $\sigma\approx 12$  [/m] at  $Re_\infty=8.0\times 10^6$  [/m] and  $\sigma\approx 17.5$  [/m] at  $Re_\infty=14.00\times 10^6$  [/m], thus representing an increase of approximately 46%.

Additionally, at a given  $\phi$  location, the most unstable frequency of the first Mack mode or the crossflow instability did not vary notably for an increased freestream Reynolds number. However, at a given value of  $Re_{\infty}$  and various  $\phi$  locations, it can be seen that the most unstable frequency of the crossflow instability decreases slightly when  $\phi$  increases (when  $Re_{\delta_1}$  increases significantly, as shown in Figure 14). This confirms that the frequency of the highly oblique modes might depend on the values of  $Re_{\delta_1}$ . However, it is important to mention that the unstable frequency range has widened, going from 20-130 [kHz] to 20-200 [kHz]. Besides, similar observations can be made for the crossflow instability where the growth rates and the unstable frequency range increase with the Reynolds number (or  $Re_{\delta_1}$ ) value.

Finally, regarding the second Mack mode, it has been found as expected that the most unstable frequency increased for a higher Reynolds number due to a thinner boundary layer. Besides, it has also been observed that the mode is destabilized by the parameter as the growth rates increased notably from  $Re_{\infty}=8.0\times10^6$  [/m] to  $Re_{\infty}=14.00\times10^6$  [/m].

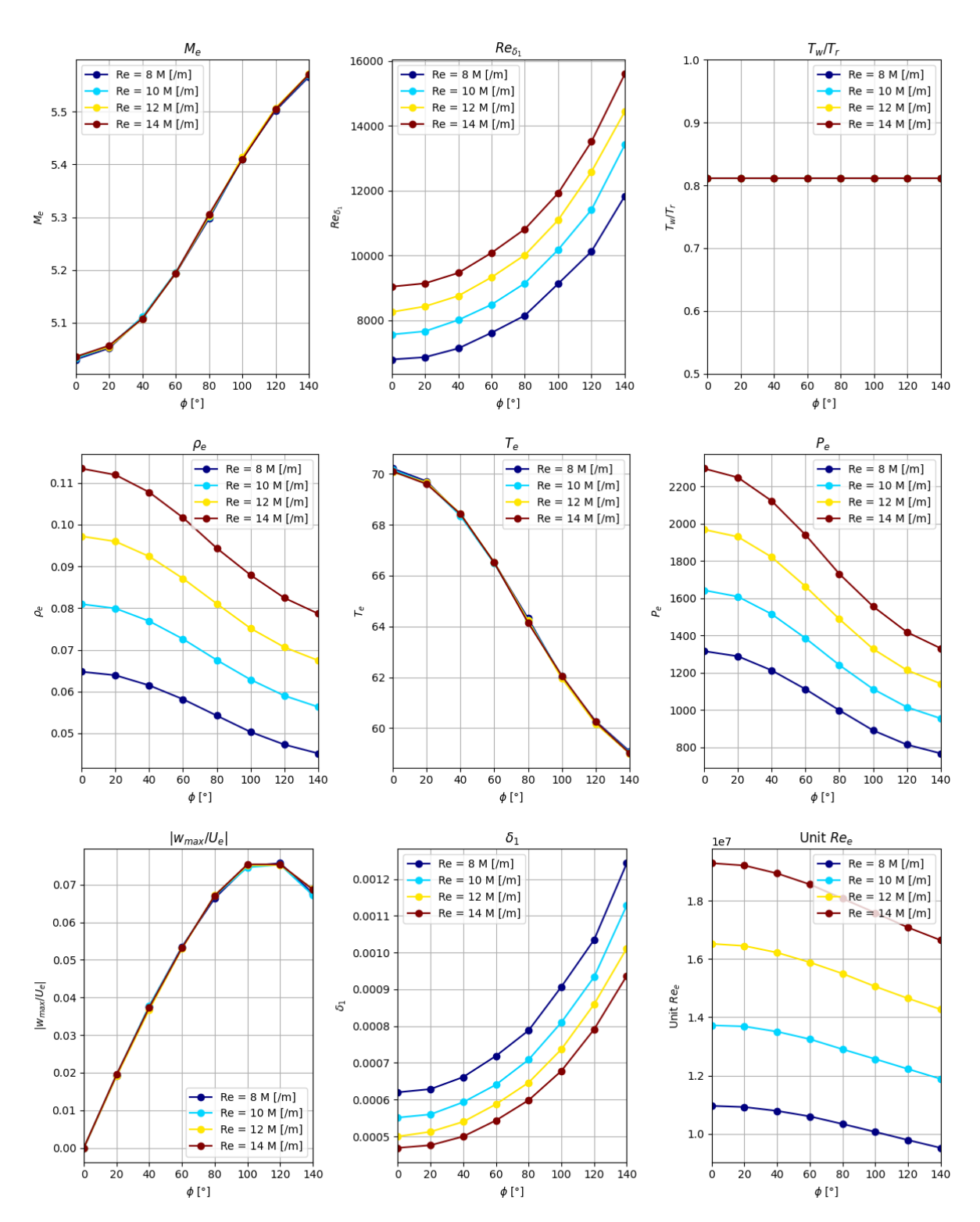


**Fig 14.** Freestream unit Reynolds number effects on the edge quantities  $M_e$ ,  $Re_{\delta_1}$ ,  $T_w/T_r$ ,  $\rho_e$ ,  $T_e$ ,  $P_e$ ,  $|w_{max}/U_e|$ ,  $\delta_1$  and  $Re_{e,unit}$  for various azimuthal angles  $\phi$  around the cone at x=0.2 [m].

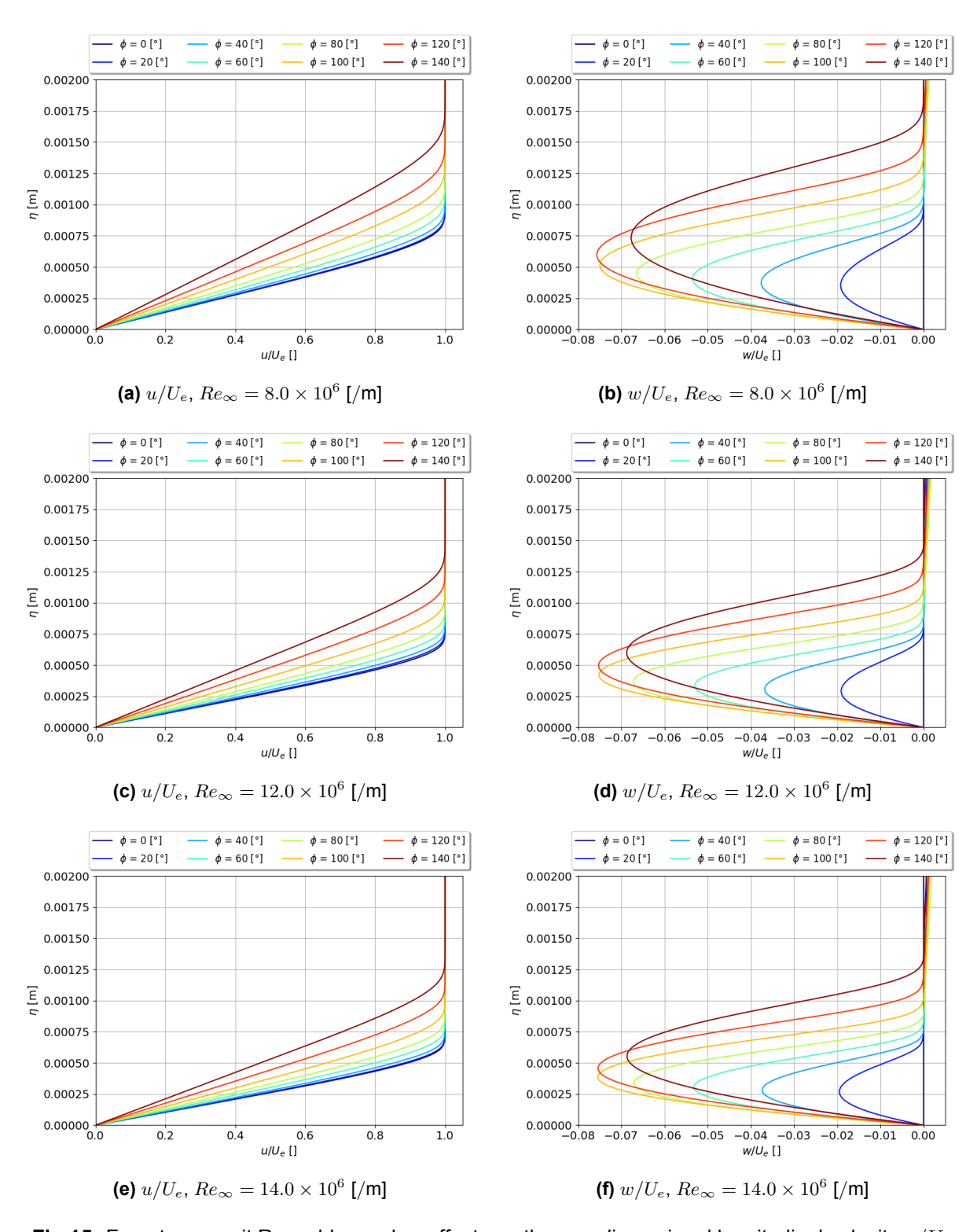
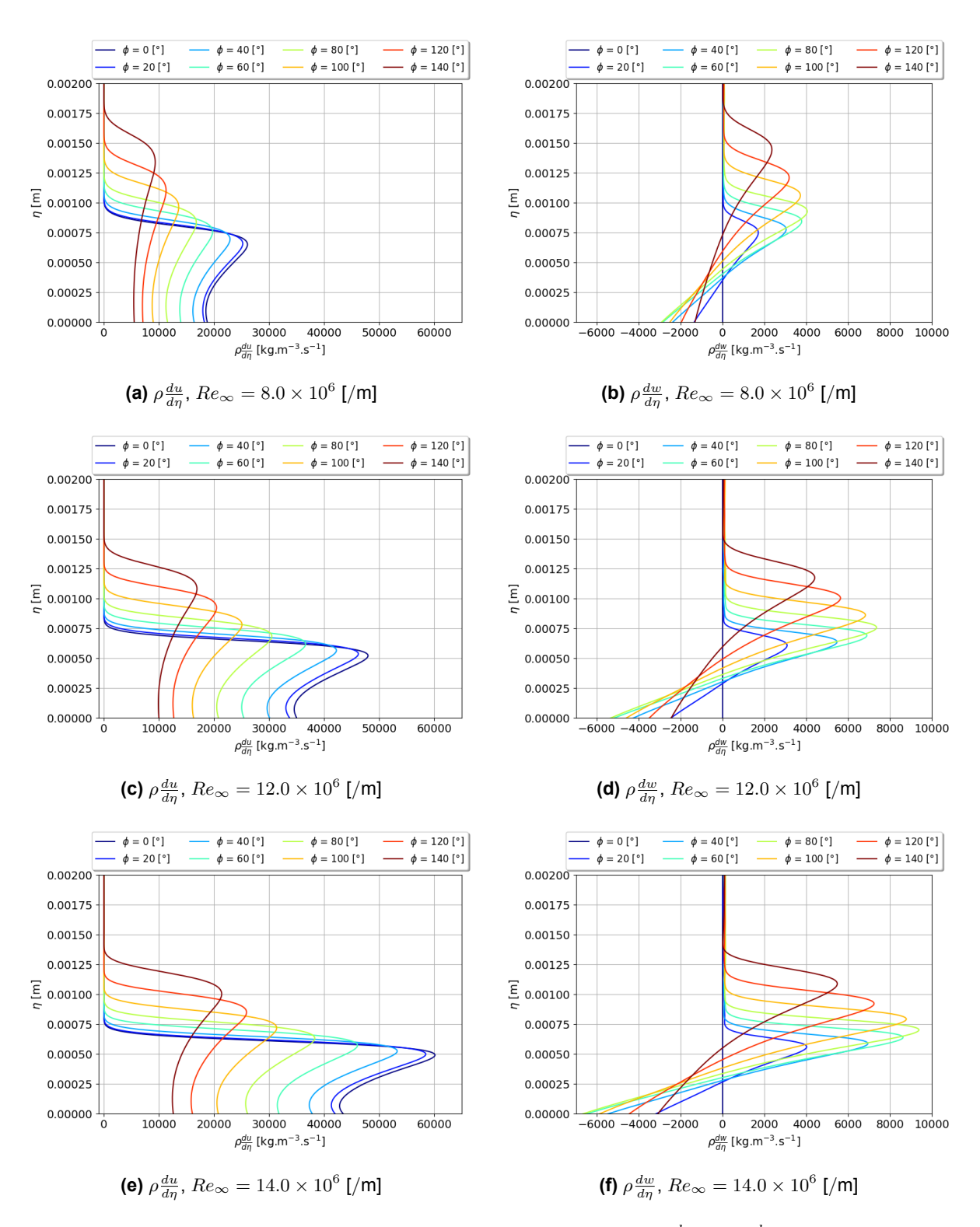
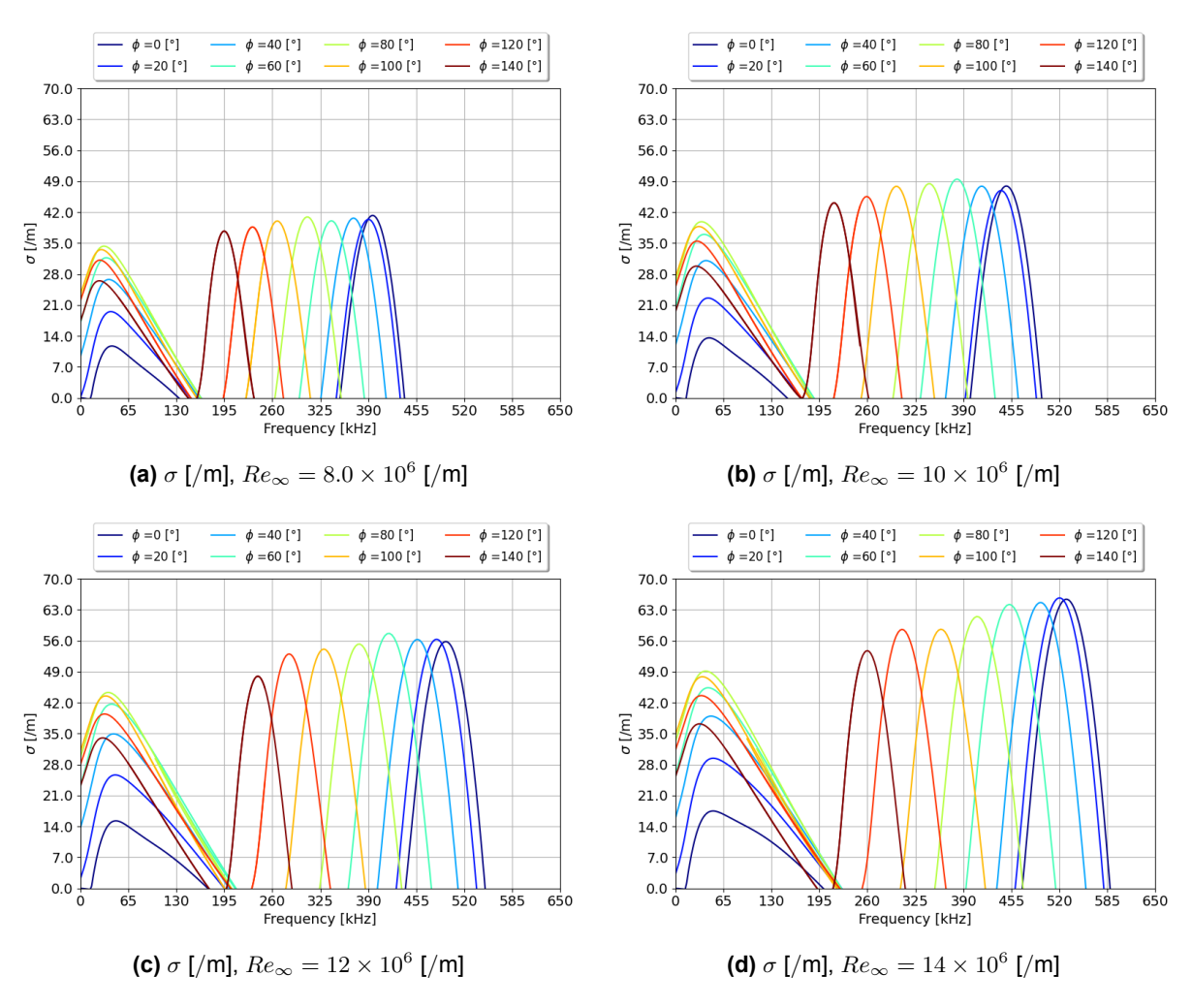


Fig 15. Freestream unit Reynolds number effects on the non-dimensional longitudinal velocity  $u/U_e$  and crossflow velocity  $w/U_e$  at x=0.2 [m] for various azimuthal angles  $\phi$  around the cone.



**Fig 16.** Freestream unit Reynolds number effects on the profiles of  $\rho \frac{du}{d\eta}$  and  $\rho \frac{dw}{d\eta}$  at x=0.2 [m] for various azimuthal angles  $\phi$  around the cone.



**Fig 17.** Freestream unit Reynolds number effects on the Mack modes and crossflow instability growth rates and frequencies at x=0.2 [m] for various azimuthal angles  $\phi$  around the cone.

### 5.3. Angle of attack effects

In this subsection, the effect of the angle of attack will be studied with fixed freestream parameters and geometry. As shown in Table 5, the angle of attack is varied from  $\alpha = 1^{\circ}$  to  $\alpha = 6^{\circ}$  with a larger increment between  $\alpha=3^{\circ}$  and  $\alpha=6^{\circ}$  to better visualize the differences in the profiles. Besides, following the conclusions taken in the previous subsection regarding the wall temperature effects, the wall temperature has been chosen high enough to make sure that the  $\rho \frac{du}{d\eta}$  and  $\rho \frac{dw}{d\eta}$  profiles all have a local extrema and consequently that all three modes are unstable.

$M_{\infty}$	$Re_{\infty}$ [/m]	<i>AoA</i> [°]	$T_w$ [K]	$T_{\infty}$ [K]	$T_{0,\infty}$ [K]	$T_w/T_r$
6.0	$10.0 \times 10^{6}$	1.0	300.0	52.00	426.4	0.8115
6.0	$10.0\times10^6$	2.0	300.0	52.00	426.4	0.8115
6.0	$10.0 \times 10^{6}$	3.0	300.0	52.00	426.4	0.8115
6.0	$10.0 \times 10^{6}$	6.0	300.0	52.00	426.4	0.8115

**Table 5.** Flow conditions considered for the study on the angle of attack effects.

Firstly, edge quantities are plotted in Figure 18 at x=0.2 [m] for various  $\phi$  locations. It has been observed that the angle of attack widened significantly the range of values of each quantity. Besides, the longitudinal velocity can be plotted for each case. As presented in Figure 19, it has been found, at a given angle of attack, that the boundary layer thickness increases when  $\phi$  increases. However, when the angle of attack is increased, it decreases for low values of  $\phi$  but increases for high values of  $\phi$ , thus leading to a wide range of values for  $\delta$  at high angles of attack (varying from  $\delta \approx 0.0007$  [m] at  $\phi = 0^{\circ}$  to  $\delta \approx 0.0019$  [m] at  $\phi = 140^{\circ}$ ). These variations of boundary layer thickness will directly be related to the unstable frequency range of the second Mack mode, known to be highly dependent on the value of  $\delta$ . Indeed, Figure 21 shows that, as the angle of attack and the variation of  $\delta$  in terms of  $\phi$  is increased, the range of unstable frequencies for the second Mack mode widens notably from 200-400 [kHz] to 140 - 600 [kHz].

Secondly, the crossflow velocity is also plotted in Figure 19. For all the chosen angles of attack, the absolute maximum value of  $w/U_e$ , noted  $|w_{max}/U_e|$ , increases when  $\phi$  increases but decreases after a threshold value of  $\phi_t$  which is approximately  $\phi_t = 100^\circ$  at  $\alpha = 1^\circ$  but  $\phi_t = 120^\circ$  at  $\alpha = 6^\circ$ . This is logical because the crossflow velocity must be zero in the symmetry planes ( $\phi = 0^{\circ}$  and  $\phi = 180^{\circ}$ ) but strictly nonzero for the other values of  $\phi$ . Moreover, it has also been found that an increase in angle of attack resulted in an increase in  $|w_{max}/U_e|$ , varying from  $|w_{max}/U_e| \approx 3\%$  at  $\alpha=1^\circ$  to  $|w_{max}/U_e| \approx 13.5\%$ at  $\alpha=6^{\circ}$ . As expected, and in addition to the previous observation, this quantitatively confirms that the angle of attack amplifies the three-dimensional effects. Indeed, these 3D effects can also be measured using the profiles of  $\rho \frac{du}{d\eta}$  and  $\rho \frac{dw}{d\eta}$ . As shown in Figure 20, it can be visualized that the values of  $(\rho\,du/d\eta)|_{\eta=0}$  and  $\max\left(\rho\frac{\mathrm{d}u}{\mathrm{d}\eta}\right)$  increase tremendously at a given  $\phi$  location when the angle of attack is increased. Moreover, when looking at the values of  $(\rho\,dw/d\eta)|_{\eta=0}$  and  $(\rho\,dw/d\eta)|_{\eta=GIP_w}$ , it appears evident that the angle of attack clearly affects both the near-wall and outer region of the boundary layer profiles.

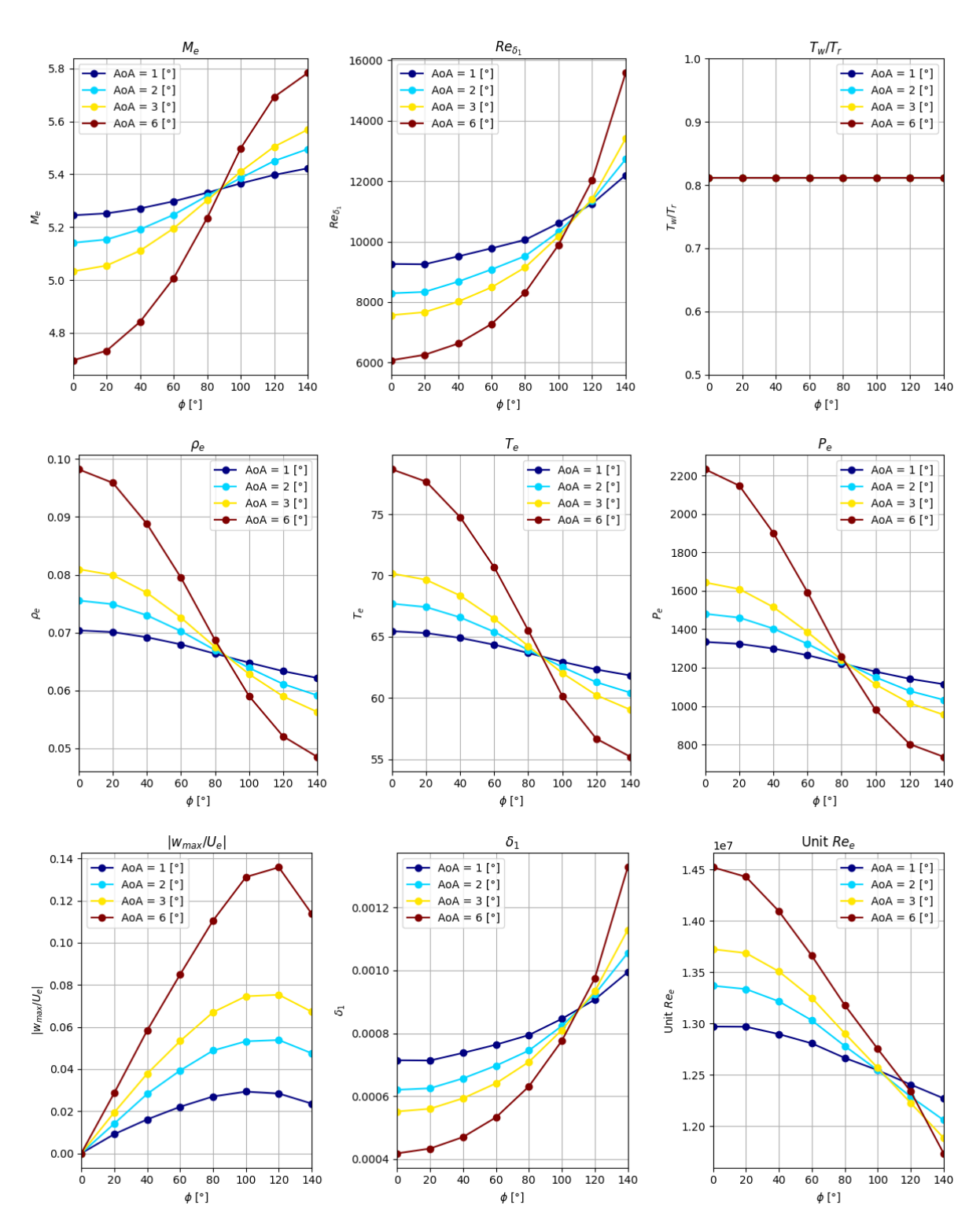


Fig 18. Angle of attack effects on the edge quantities  $M_e$ ,  $Re_{\delta_1}$ ,  $T_w/T_r$ ,  $\rho_e$ ,  $T_e$ ,  $P_e$ ,  $|w_{max}/U_e|$ ,  $\delta_1$  and  $Re_{e,unit}$  for various azimuthal angles  $\phi$  around the cone at x=0.2 [m] along the cone.

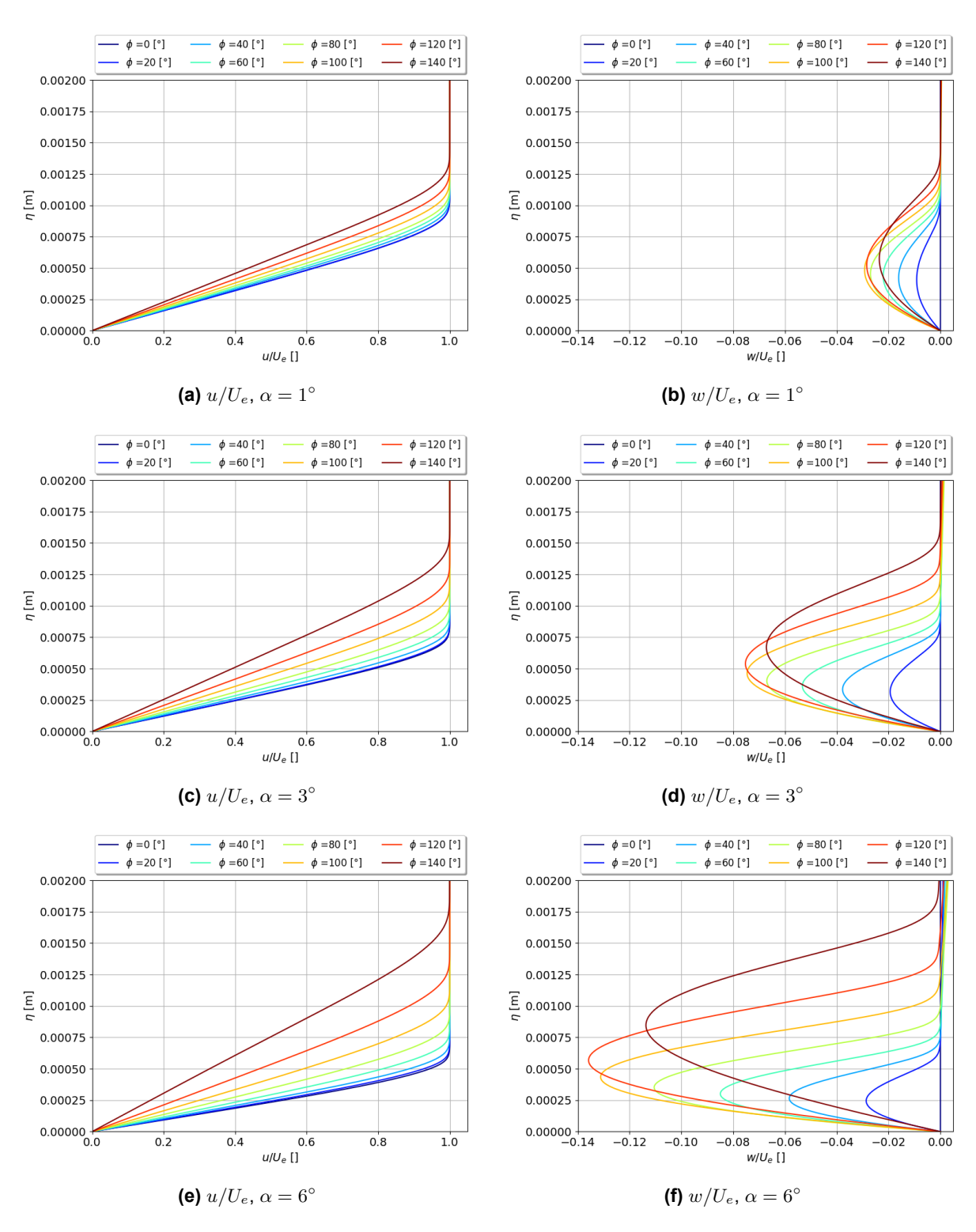
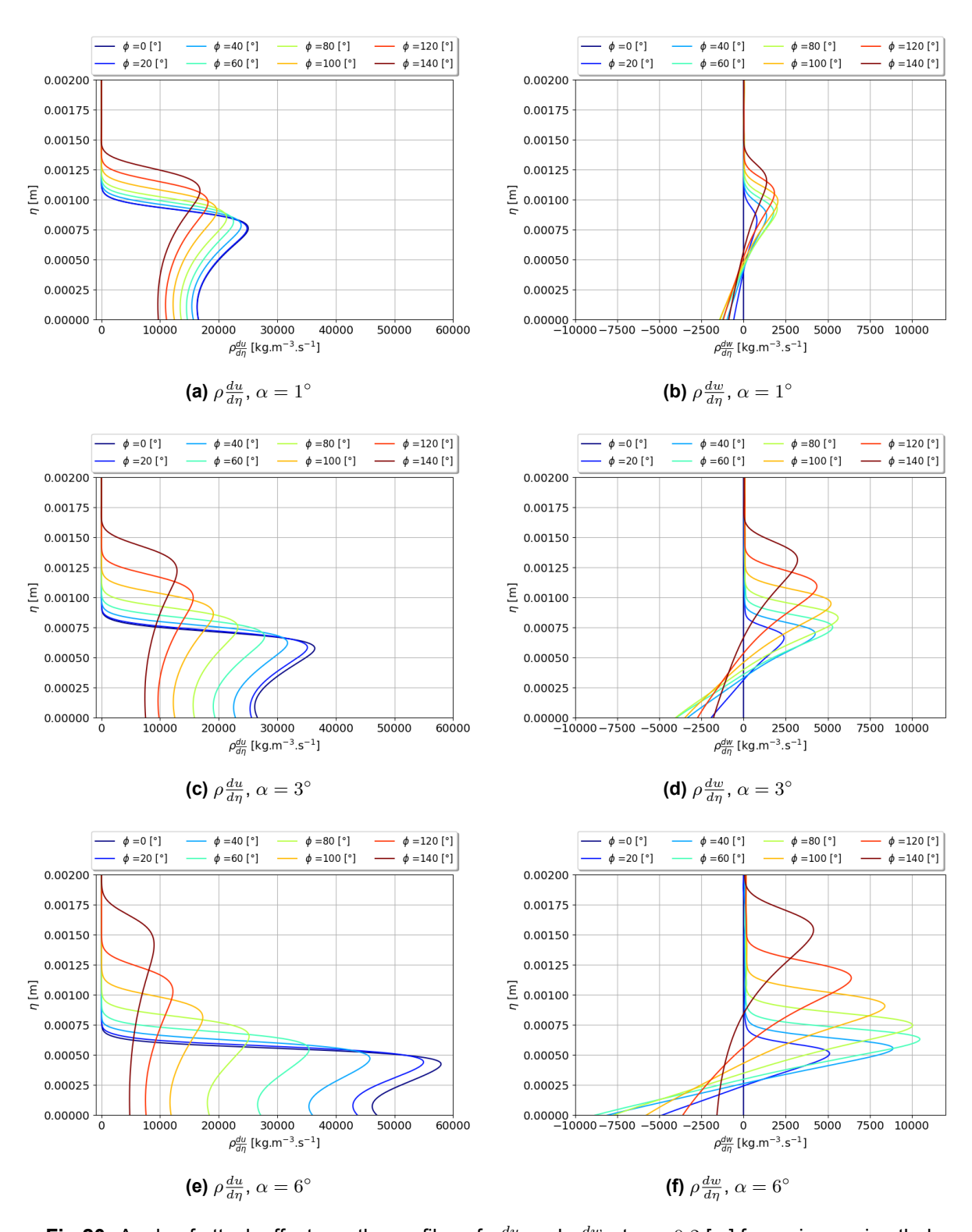


Fig 19. Angle of attack effects on the non-dimensional longitudinal velocity  $u/U_e$  and crossflow velocity  $w/U_e$  at x=0.2 [m] for various azimuthal angles  $\phi$  around the cone.



**Fig 20.** Angle of attack effects on the profiles of  $\rho \frac{du}{d\eta}$  and  $\rho \frac{dw}{d\eta}$  at x=0.2 [m] for various azimuthal angles  $\phi$  around the cone.

Finally, regarding the stability results, the growth rate is plotted in terms of the frequency in Figure 21 for various boundary layer profiles around the cone at x = 0.2 [m]. Generally, it has been found that an increased angle of attack strongly destabilized the crossflow instability which became dominant over the second Mack mode at high angles of attack for the considered freestream flow conditions. Moreover, although it appears more subtle at  $\alpha=1^{\circ}$ , it appears evident at  $\alpha=3^{\circ}$  or  $\alpha=6^{\circ}$  that the dominant frequency of the crossflow mode decreases when  $\phi$  increases. However, considering that the values of  $M_e$ ,  $T_e$ ,  $U_e$ ,  $Re_{\delta_1}$  and  $|w_{max}/U_e|$  change at each  $\phi$  location, it is challenging to interpret this behavior. Then, regarding the first Mack mode at  $\phi = 0^{\circ}$ , it has unexpectedly been found that, despite values of  $M_e,\,T_e,\,U_e$  but also  $\rho \frac{du}{d\eta}$  that vary significantly when increasing the angle of attack (see Figure 18), the growth rate stayed at a roughly constant value of  $\sigma \approx 13$  [/m] and a most unstable frequency of  $f \approx 45$  [kHz].

Regarding the second Mack mode, it has been found at  $\alpha=1^\circ$  that the growth rates are roughly constant for all values of  $\phi$  due to the fact that the values of  $M_e$ ,  $T_e$ ,  $U_e$  are fairly unchanged as well and that the three-dimensionality of the flow is weak ( $|w_{max}/U_e|$  is small). However, when the angle of attack is increased, it has generally been found that the growth rates tended to decrease slightly until  $lpha=6^\circ$ where it was more pronounced at  $\phi \leq 60^{\circ}$  only. This is possibly due to the fact that, going from  $\alpha = 3^{\circ}$ to  $\alpha=6^{\circ}$ , the variation of edge quantities was found to be the highest at  $\phi \leq 60^{\circ}$ .

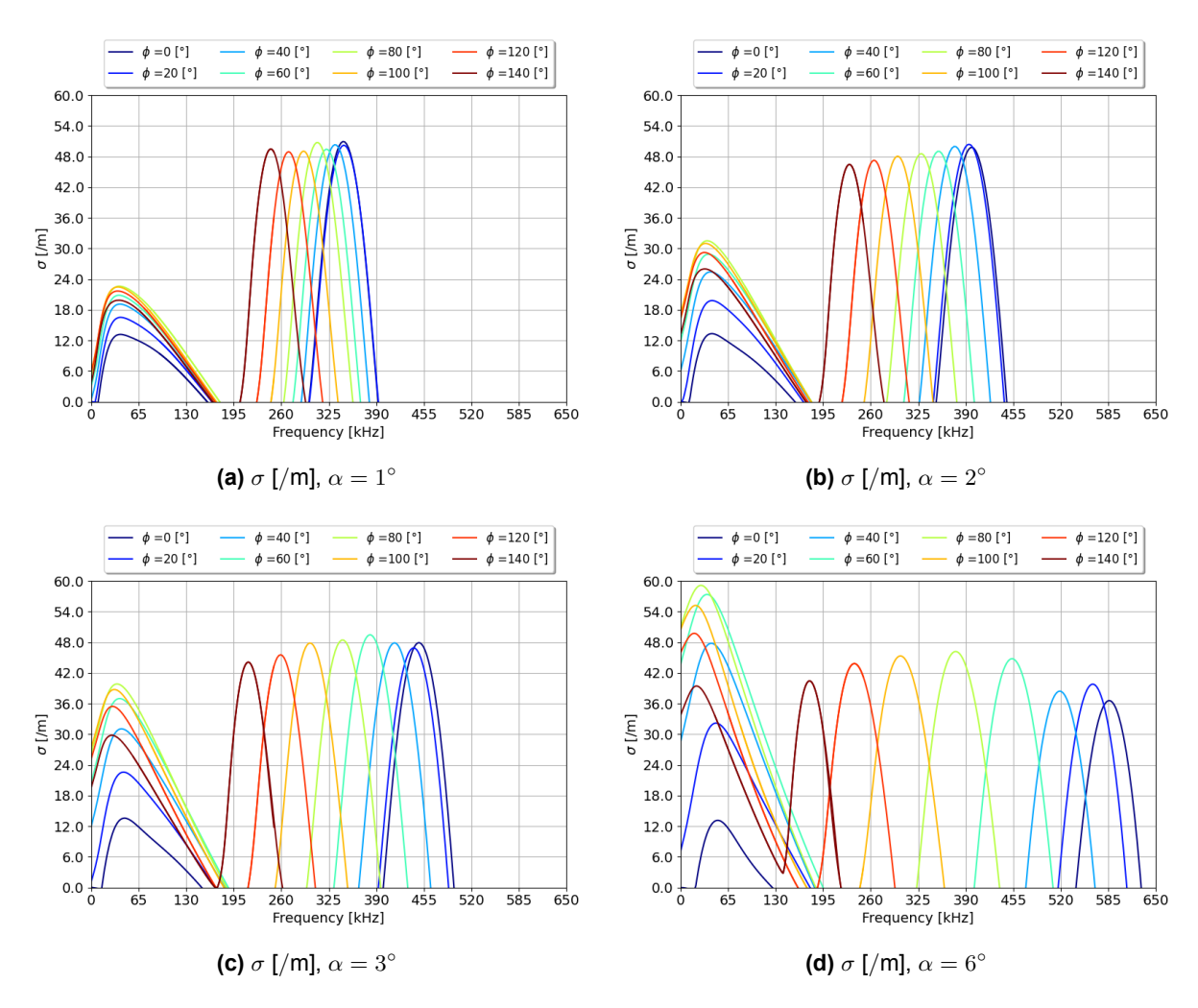


Fig 21. Angle of attack effects on the Mack modes and crossflow instability growth rates and frequencies at x=0.2 [m] for various azimuthal angles  $\phi$  around the cone.

## 6. Conclusions and perspectives

In this paper, a feature-based mesh adaptation methodology has been validated to reproduce boundary layer profiles and their derivatives, stability diagrams on isolated boundary layer profiles and N-factors along a given streamline. It has been used to study the effect of some flow parameters such as the unit Reynolds number  $Re_{\infty}$ , the angle of attack  $\alpha$  and the wall temperature ratio  $T_w/T_r$  on the profiles and the typical instability waves (Mack modes and crossflow instability) that lead to transition. This paper thus provides an insight into their effects and a first glimpse at pertinent boundary layer quantities that would help to characterize and model more effectively these modes in a wide range of flow conditions. For instance, it seemed that the most unstable frequency of the crossflow instability was highly related to the value of  $Re_{\delta_1}$ , similarly to the first Mack mode.

Regarding the effect of the wall-to-recovery temperature ratio  $T_w/T_r$ , it was found to significantly change the boundary layer profiles and thus the growth rates and frequencies of the instability waves. As  $T_w/T_r$  increased, the second Mack mode was less unstable whereas the first Mack mode and the crossflow instability became notably more unstable. Although the first Mack mode can be completely stable at low values of  $T_w/T_r$  due to the absence of a generalized inflexion point for the longitudinal velocity, the crossflow instability was found to always be unstable due to the necessary presence of a generalized inflexion point on the crossflow velocity when it is not zero. It is also worth mentioning that LST always predicts a higher growth rate for the traveling (f>0 [Hz]) crossflow mode compared to its stationary (f=0 [Hz]) counterpart. Moreover, as  $T_w/T_r$  increased, the boundary layer thickened and the most unstable frequency of the second Mack mode decreased. Besides, a significant displacement effect was measured using values of  $\delta_1$  when  $T_w/T_r$  increased.

Regarding the effect of the Reynolds number, it has unsurprisingly been observed that the higher the value, the more unstable these modes will be and the more upstream the transition will be expected. Besides, it has been found that the most unstable frequency of the second Mack mode is highly sensitive to the boundary layer thickness  $\delta$ . However, a deeper study on the effect of  $Re_{\delta_1}$  must be conducted in order to quantify its effect on the most unstable frequency of the crossflow instability.

Finally, regarding the effect of the angle of attack, it has been found to strongly affect the boundary layer profiles and quantities such as  $\delta$ ,  $M_e$ ,  $T_e$  and  $|w_{max}/U_e|$ . Besides, the variation of these parameters was highly dependent on the values of  $\phi$  (i.e. on the position around the cone where the boundary layer profile was taken), thus highlighting significant three-dimensional effects. As a result, it has been shown that the angle of attack significantly destabilizes the crossflow instability while its effect on the Mack modes' growth rates were found to be moderately stabilizing. However, due to a wider range of  $\delta$  values, the unstable frequency range of the second Mack mode has been observed to widen drastically as the angle of attack was increased.

In future work, the generated database of boundary layer profiles and stability results will be used to improve correlations in RANS-based transition models.

# 7. Acknowledgments

The author gratefully acknowledges the developers of the CFD solver SoNICS (ONERA-Safran property) [11] for their support.

#### References

- [1] P. Paredes, B. Venkatachari, M. M. Choudhari, F. Li, C.-L. Chang, M. I. Zafar, and H. Xiao, "Toward a practical method for hypersonic transition prediction based on stability correlations," *AIAA Journal*, vol. 58, no. 10, pp. 4475–4484, 2020.
- [2] T. J. Juliano, M. P. Borg, and S. P. Schneider, "Quiet tunnel measurements of HIFiRE-5 boundary-layer transition," *AIAA Journal*, vol. 53, no. 4, pp. 832–846, 2015.
- [3] L. Mack, "Special course on stability and transition of laminar flow," AGARD Special Course at the von Karman Institute, 1984.
- [4] A. Loseille and F. Alauzet, "Continuous mesh framework part I: Well-posed continuous interpolation error," *SIAM Journal on Numerical Analysis*, vol. 49, no. 1, pp. 38–60, 2011.
- [5] A. Loseille and F. Alauzet, "Continuous mesh framework part II: Validations and applications," *SIAM Journal on Numerical Analysis*, vol. 49, no. 1, pp. 61–86, 2011.
- [6] F. Alauzet and G. Olivier, "Extension of metric-based anisotropic mesh adaptation to time-dependent problems involving moving geometries," in 49th AIAA Aerospace Sciences Meeting, (Orlando), AIAA Paper 2011-896, 2011.
- [7] P.-L. George, F. Hecht, and M.-G. Vallet, "Creation of internal points in Voronoi's type method," *Advances in Engineering Software and Workstations*, vol. 13, no. 5, pp. 303–312, 1991.
- [8] D. Arnal and G. Casalis, "Laminar-turbulent transition prediction in three-dimensional flows," Progress in Aerospace Sciences, vol. 36, no. 2, pp. 173–191, 2000.
- [9] M. A. Park, Anisotropic output-based adaptation with tetrahedral cut cells for compressible flows.
   PhD thesis, Massachusetts Institute of Technology, 2008.
- [10] M. A. Park, A. Balan, F. Clerici, F. Alauzet, A. Loseille, D. S. Kamenetskiy, J. A. Krakos, T. R. Michal, and M. C. Galbraith, "Verification of viscous goal-based anisotropic mesh adaptation," in AIAA Scitech 2021 Forum, AIAA Paper 2021-1362, 2021.
- [11] D. Gueyffier, S. Plot, and M. Soismier, "SoNICS: a new generation CFD software for satisfying industrial users needs," in *OTAN/STO/Workshop AVT-366*, May 2022.
- [12] A. Dervieux, "Steady Euler simulations using unstructured meshes," in *Partial Differential Equations* of *Hyperbolic Type and Applications*, pp. 33–111, 1987.
- [13] P. Rostand and B. Stoufflet, "Finite volume Galerkin methods for viscous gas dynamics," Tech. Rep. RR-0863, INRIA, 1988.
- [14] S. Liu, B. Wan, X. Yuan, L. Zhang, J. Chen, and X. Chen, "Linear modal global instabilities of hypersonic flow over an inclined cone," *Physics of Fluids*, vol. 34, no. 7, p. 074108, 2022.
- [15] F. Li, M. Choudhari, C.-L. Chang, J. White, R. Kimmel, D. Adamczak, M. Borg, S. Stanfield, and M. Smith, "Stability analysis for HIFiRE experiments," in 42nd AIAA Fluid Dynamics Conference and Exhibit, AIAA Paper 2012-2961, 2012.
- [16] M. Borg, R. Kimmel, and S. Stanfield, "HIFiRE-5 attachment-line and crossflow instability in a quiet hypersonic wind tunnel," in 41st AIAA Fluid Dynamics Conference and Exhibit, AIAA Paper 2011-3247, 2011.
- [17] Q. Wang, X. Xiang, S. Dong, X. Yuan, J. Chen, and X. Chen, "Wall temperature effects on the hypersonic boundary-layer transition over an inclined blunt cone," *Physics of Fluids*, vol. 35, no. 2, p. 024107, 2023.